

Physics-based Modeling and Scalable Optimization of Large Intelligent Reflecting Surfaces

Marzieh Najafi, *Student Member, IEEE*, Vahid Jamali, *Member, IEEE*,
Robert Schober, *Fellow, IEEE*, and Vincent H. Poor, *Fellow, IEEE*

Abstract

Intelligent reflecting surfaces (IRSs) have the potential to transform wireless communication channels into smart reconfigurable propagation environments. To realize this new paradigm, the passive IRSs have to be large, especially for communication in far-field scenarios, so that they can compensate for the large end-to-end path-loss, which is caused by the multiplication of the individual path-losses of the transmitter-to-IRS and IRS-to-receiver channels. However, optimizing a large number of sub-wavelength IRS elements imposes a significant challenge for online transmission. To address this issue, in this paper, we develop a physics-based model and a scalable optimization framework for large IRSs. The basic idea is to partition the IRS unit cells into several subsets, referred to as tiles, model the impact of each tile on the wireless channel, and then optimize each tile in two stages, namely an offline design stage and an online optimization stage. For physics-based modeling, we borrow concepts from the radar literature, model each tile as an *anomalous* reflector, and derive its impact on the wireless channel for a given phase shift by solving the corresponding integral equations for the electric and magnetic vector fields. In the offline design stage, the IRS unit cells of each tile are jointly designed for the support of different transmission modes, where each transmission mode effectively corresponds to a given configuration of the phase shifts that the unit cells of the tile apply to an impinging electromagnetic wave. In the online optimization stage, the best transmission mode of each tile is selected such that a desired quality-of-service (QoS) criterion is maximized. We consider an exemplary downlink system and study the minimization of the base station (BS) transmit power subject to QoS constraints for the users. Since the resulting mixed-integer programming problem for joint optimization of the BS beamforming vectors and the tile transmission modes is non-convex, we derive two efficient suboptimal solutions, which are based on alternating optimization and a greedy approach, respectively. We show that the proposed modeling and optimization framework can be used to efficiently optimize large IRSs comprising thousands of unit cells.

This paper has been submitted in part for presentation at the Asilomar Conference on Signals, Systems, and Computers 2020 [1].

M. Najafi, V. Jamali, and R. Schober are with the Institute for Digital Communications at Friedrich-Alexander University Erlangen-Nürnberg (FAU) (e-mail: marzieh.najafi@fau.de; vahid.jamali@fau.de; robert.schober@fau.de).

H. Vincent Poor is with the Department of Electrical Engineering, Princeton University, Princeton, NJ 08544 USA (e-mail: poor@princeton.edu).

I. INTRODUCTION

Smart wireless environments are a newly emerging concept in wireless communications where intelligent reflecting surfaces (IRSs) are deployed to influence the propagation characteristics of the wireless channel [2], [3]. IRSs consist of a large number of programmable sub-wavelength elements, so-called unit cells or meta atoms, that can change the properties of an impinging electromagnetic (EM) wave while reflecting it. For instance, a properly designed unit cell phase distribution across the surface enables the IRS to alter the direction of the wavefront of the reflected wave, thereby realizing the generalized Snell's law [4], [5]. Moreover, since the unit cells are passive and cost-efficient, it is expected that *large* IRSs comprising hundreds if not thousands of unit cells can be manufactured and deployed to assist a link [6]–[8]. Proof-of-concept implementations confirming the benefits of IRSs have been reported in [8]–[10].

A. State-of-the-Art Approach to IRS Optimization

Let us consider an IRS with Q unit cells. A widely-adopted model for IRSs in the literature is to assume that each unit cell individually acts as a diffusive scatterer which is able to change the phase of the impinging EM wave, i.e., $E_{r,q} = E_{t,q}e^{j\beta_q}$, where $E_{t,q}$ and $E_{r,q}$ denote the incident and reflected scalar electric fields of the q -th unit cell, respectively, and $\beta_q \in \mathcal{B} \subset [0, 2\pi)$ is the phase change applied by the q -th unit cell with values from set \mathcal{B} [6], [7], [11]. The IRS is configured by optimizing the β_q which leads to non-convex optimization problems due to the unit-modulus constraint imposed by $|e^{j\beta_q}| = 1$, see [6], [7], [11]–[15] for different approaches to cope with this non-convex constraint. Unfortunately, these optimization methods are not scalable for large IRSs as the number of optimization variables becomes unmanageably large. For example, assuming a unit-cell spacing of half a wavelength, a 1 m-by-1 m IRS would comprise $Q = 1100$ unit cells for a carrier frequency of 5 GHz. Therefore, the direct optimization of $\beta_q, \forall q$, may not be a feasible approach for the online design of large IRSs.

Moreover, as the physics-based models in [16]–[18] suggest, the path-loss of the end-to-end IRS-assisted links is significant for *far-field* scenarios and indeed a *very large* IRS is needed to overcome it in practice. To see this, let ρ_d , ρ_t , and ρ_r denote the transmitter-to-receiver, transmitter-to-IRS, and IRS-to-receiver distances, respectively. Thereby, assuming free-space propagation, the path-losses of the direct and IRS-assisted links are proportional to $\frac{1}{4\pi\rho_d^2}$ and $\frac{A^2}{4\pi\lambda^2\rho_t^2\rho_r^2}$, respectively, where λ is the wavelength and A is the area of the IRS, see [16] and Corollaries 1, 2, and Remark 2 for details. Therefore, for the unobstructed direct and IRS-assisted links to have similar path-losses, the normalized size of the IRS has to scale as $\frac{A}{\lambda^2} \propto \frac{\rho_t\rho_r}{\rho_d\lambda}$. For example, assuming $\rho_d = 200$ m, $\rho_t = \rho_r = 100$ m, and a unit-cell

spacing of half a wavelength, $Q \propto \frac{200}{\lambda} \approx 3300$ unit cells are needed for a carrier frequency of 5 GHz. We note that the main reason why many existing works, e.g., [6], [11], [19], report performance gains for IRSs with much smaller numbers of unit cells (e.g., on the order of tens of unit cells) is the use of link models which do not include all the losses for far-field scenarios and/or an exceedingly weak direct link, see also [16]. Other existing works consider a small number of IRS elements but assume that each element is able to provide an effective *constant gain* that is *implicitly* incorporated in the channel gain [14], [15], [20]. Such elements, which we refer to as tiles, can be realized and are larger than the wavelength or are comprised of several sub-wavelength unit cells [14]. However, the gain provided by these tiles is not constant and depends on several factors such as the angle of incident, the angle of reflection/observation, and the polarization of the impinging wave. A physics-based model that accounts for these factors is essential to properly model the signals and interference at the receivers of a wireless system. In particular, a large gain implies highly directive tiles which means that a receiver that is not located close to the main lobe of the radiation pattern of these tiles will receive negligible power. Hence, any further attempt to constructively combine the negligible powers arriving from different tiles by configuring the phase shifts of the tiles will lead to an inefficient solution. Therefore, the development of a physics-based end-to-end channel model for *large IRSs* that accounts for all relevant effects and allows for the *scalable optimization* of the IRS configuration is of utmost importance.

B. Proposed Modeling and Optimization Framework for IRS

In this paper, we develop a scalable optimization framework for large IRSs, which is rooted in a physics-based IRS channel model and provides a tunable tradeoff between performance and complexity. The basic idea is to partition the IRS unit cells into $N \ll Q$ tiles. We then model the impact of a tile on the wireless channel for a given phase-shift configuration of the unit cells of the tile. Using this model, we optimize the tile configuration in two stages, namely an offline design and an online optimization stage.

Physics-based Model for IRS-Assisted Channel: Borrowing an analogy from the radar literature, we model each tile as an *anomalous* reflector. Hence, for a given configuration of the unit cell phase shifts, which we refer to as a transmission mode, and assuming a far-field scenario, a tile is characterized by a response function $g(\Psi_t, \Psi_r)$. The tile response function is essentially a generalization of the radar cross section (RCS) of an object [21] and accounts for both the amplitude and phase of the reflected EM wave. More specifically, the tile response function determines how a plane wave impinging from direction Ψ_t with a given polarization is reflected in direction Ψ_r for a given phase-shift configuration

of the unit cells of the tile. We derive $g(\Psi_t, \Psi_r)$ by solving the corresponding integral equations for the electric and magnetic vector fields [21]. In particular, we first derive $g(\Psi_t, \Psi_r)$ for ideal continuous tiles with programmable surface impedance. Exploiting this result, we then derive $g(\Psi_t, \Psi_r)$ for discrete tiles consisting of sub-wavelength unit cells. We show that discrete tiles with a unit-cell spacing of less than $\lambda/2$ can accurately approximate continuous tiles. Furthermore, we model the IRS-assisted end-to-end channel between multiple transmitters and multiple receivers as a function of the response functions $g(\Psi_t, \Psi_r)$ of all tiles of the IRS where each tile is set to support a given transmission mode. This general model includes as special cases point-to-point, multiuser uplink and downlink, and multi-cell communication channels and accounts for the existence of multiple scatterers in the environment.

We note that the physics-based model derived in this paper generalizes the models in [16]–[18] which provide interesting insights, but were obtained under more restrictive assumptions. For instance, in [16], the scatter field was characterized for a specific polarization and the angles of the impinging and reflected waves were in the same plane, see Remark 1. However, in practice, several waves may impinge on the same IRS from different directions and with different polarizations and will be redirected in different directions. In [17], the authors studied the power scaling laws for asymptotically large IRSs; however, similar to [16], general incident and reflection directions were not considered. Furthermore, in [18], the authors modeled an IRS in a *two-dimensional* system using the *scalar* theory of diffraction and the Huygens-Fresnel principle. In this paper, we consider a three-dimensional system and by analyzing the electric and magnetic vector fields, we characterize the reflected wave for all observation angles when a plane wave with arbitrary incident angle and arbitrary polarization impinges on the IRS.

Offline Design: The unit cells of each tile are jointly designed offline to provide M different transmission modes, i.e., M different phase-shift configurations. In general, the capabilities of the transmission modes may range from changing the direction of the wavefront to splitting the incoming wave into multiple directions or scattering the wave. However, in this paper, we focus on transmission modes that enable the generalized Snell’s law, i.e., change the direction of the reflected wavefront [4], [5], [22]. To this end, we design an offline codebook of transmission modes, which is the product of three component codebooks, namely two *reflection* codebooks that jointly enable the tile to reflect an incident wave along desired elevation and azimuth angles and a *wavefront phase* codebook which enables constructive/destructive superposition of the waves that arrive from different tiles at the receivers.

Online Optimization: In the online optimization stage, the objective is to select for each fading realization the best transmission mode for each tile such that a desired quality-of-service (QoS) criterion is maximized. The resulting optimization problems are in the form of *mixed integer programming*

[23]–[25]. We emphasize that, for a given channel realization, it may not be necessary to use all transmission modes in the offline codebook for online optimization. In fact, to reduce the complexity of online optimization, we propose to select a subset \mathcal{M} of transmission modes, e.g., those modes that yield a non-negligible signal power at the intended receivers. This reduces the search space for online optimization from $|\mathcal{B}|^Q$ for the naive approach which directly optimizes the phase shifts of the unit cells, $\beta_q \in \mathcal{B}, \forall q$, to $|\mathcal{M}|^N$, where the number of modes $|\mathcal{M}|$ and the number of tiles N are design parameters that can be selected by the system designer to trade performance for complexity.

For concreteness, we focus on a downlink communication system where a multiple-antenna base station (BS) serves multiple single-antenna users. We assume that the direct link exists but may be severely shadowed/blocked and hence an IRS is deployed to improve the communication. For this system, we jointly optimize the IRS and the precoder at the BS to minimize the transmit power of the BS while guaranteeing a minimum QoS for the users. Since the formulated problem is non-convex, we develop two efficient suboptimal solutions. The first solution exploits well-known techniques such as alternating optimization (AO), big-M formulation, and semidefinite programming, whereas the second solution is greedy and configures the tiles and the precoder in an iterative manner while ensuring that the transmit power is reduced in each iteration. Finally, we use computer simulations to quantify the impact of the number of unit cells, number of tiles, blockage of the direct link, and the position of the IRS on the system performance. In particular, we show that the proposed optimization framework can be used to configure IRSs with thousands of unit cells by grouping them into a small number of tiles (on the order of few tens) without significant performance degradation.

The remainder of this paper is organized as follows. In Section II, we present the proposed physics-based model for continuous and discrete tiles as well as the end-to-end channel model for IRS-assisted wireless systems. In Section III, we first design an offline codebook for the transmission modes of the tiles. Subsequently, we formulate and solve an online optimization problem. Simulation results are presented in Section IV, and conclusions are drawn in Section V.

II. END-TO-END CHANNEL MODEL FOR IRS-ASSISTED WIRELESS SYSTEMS

In this section, we first present the considered IRS structure. Subsequently, we model both continuous and discrete IRS tiles by deriving the corresponding tile response functions for given transmission modes. Exploiting these results, we then develop the proposed end-to-end channel model for IRS-assisted wireless systems.

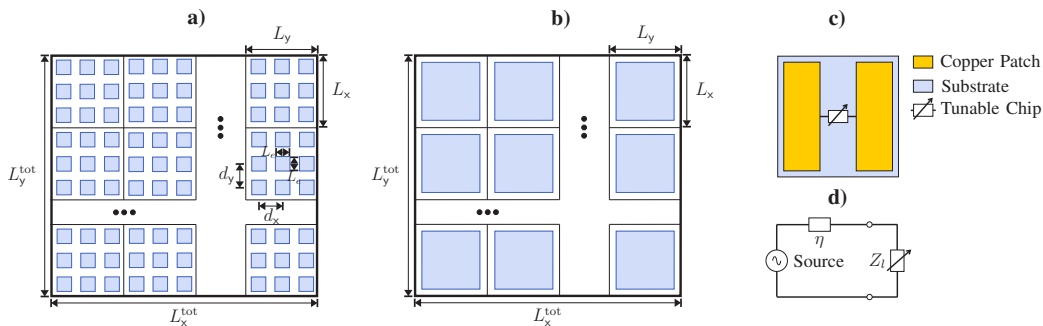


Fig. 1. Schematic illustration of planar IRS of size $L_x^{\text{tot}} \times L_y^{\text{tot}}$ partitioned into tiles of size $L_x \times L_y$. a) Each tile is composed of square unit cells of size $L_e \times L_e$ which are spaced by d_x and d_y along the x and y directions, respectively. b) Each tile may be approximated as a continuous surface. c) Schematic illustration of tunable unit cells. d) Equivalent circuit model for the unit cells, see [5], [26], [27] for various implementations of the tunable chip.

A. IRS Structure

We consider a large rectangular IRS of size $L_x^{\text{tot}} \times L_y^{\text{tot}}$ placed in the $x-y$ plane where $L_x^{\text{tot}}, L_y^{\text{tot}} \gg \lambda$, see Fig. 1. The IRS is composed of many sub-wavelength unit cells (also known as meta atoms) of size $L_e \times L_e$ that are able to change the properties of an impinging EM wave when reflecting it. Typically, each unit cell contains programmable components (such as tunable varactor diodes or switchable positive-intrinsic-negative (PIN) diodes) that can change the reflection coefficient of the surface, which we denote by Γ , see Fig. 1 c).

We assume that the IRS is partitioned into tiles of size $L_x \times L_y$. For notational simplicity, let us assume that L_x^{tot}/L_x and L_y^{tot}/L_y are integers and in total, there are $N = L_x^{\text{tot}}L_y^{\text{tot}}/(L_xL_y)$ tiles. Each tile consists of several programmable sub-wavelength unit cells. Here, assuming a unit-cell spacing of d_x and d_y along the x and y axes, respectively, the total number of unit cells of the IRS is given by $Q = NQ_xQ_y$, where $Q_x = L_x/d_x$ and $Q_y = L_y/d_y$. When $d_x = d_y \approx L_e \ll \lambda$ and $L_x, L_y \gg \lambda$, the collection of all unit cells on one tile act as a continuous programmable surface [28], [29], cf. Fig. 1 b). In this paper, an ideal tile that acts as a continuous programmable surface is referred to as a *continuous tile*. In contrast, a practical tile that comprises a discrete number of unit cells is referred to as a *discrete tile*. We use the notion of continuous tiles in Section II.B to rigorously analyze the reflected EM field.

We focus on the far-field scenario where the curvature of the wavefront originating from a distant source on the tile can be neglected. Therefore, the incident EM wave can be modeled as a plane wave impinging on the tile and is characterized by $\Psi_t = (\theta_t, \phi_t, \varphi_t)$, see Fig. 2. Here, θ_t and ϕ_t denote the elevation and azimuth angles of the incident direction, respectively, and φ_t determines the polarization of the incident wave. The unit cells of the tile act as secondary sources and reflect the incident EM wave. The signal received at a receiver in the far field of the tile can be characterized by the overall

complex tile response function $g(\Psi_t, \Psi_r)$, where $\Psi_r = (\theta_r, \phi_r)$ denotes the reflection angle at which the receiver is located¹. The power of the tile response function, $|g(\Psi_t, \Psi_r)|^2$, is referred to as the RCS of an object [21, p. 584]. Here, to be able to model the superposition of multiple waves at a receiver in the far field, we generalize the concept of RCS to also include the phase information, i.e.,

$$g(\Psi_t, \Psi_r) = \lim_{\rho_r \rightarrow \infty} \sqrt{4\pi\rho_r^2} e^{-jk\rho_r} \frac{E_r(\Psi_r)}{E_t(\Psi_t)}, \quad (1)$$

where $k = \frac{2\pi}{\lambda}$ is the wave number, $E_t(\Psi_t)$ is a phasor denoting the complex amplitude of the incident electric field impinging from angle Ψ_t on the tile center (i.e., $(x, y) = (0, 0)$), and $E_r(\Psi_r)$ is a phasor denoting the complex amplitude of the reflected electric field in direction Ψ_r and at distance ρ_r from the tile center. In the following, we derive $g(\Psi_t, \Psi_r)$ for both continuous and discrete tiles for a given transmission mode. Whenever necessary, we use the superscripts c and d for the tile response function to distinguish between continuous and discrete tiles, respectively.

B. Continuous Tiles

In order to study the impact of a continuous tile on an impinging EM wave, we first explicitly define the incident electric and magnetic fields. Here, we assume the following incident fields with arbitrary polarization and incident angle [21, Ch. 11]²

$$\mathbf{E}_t(\Psi_t) = E_0 e^{jk\mathbf{a}_t \cdot (\mathbf{e}_x x + \mathbf{e}_y y + \mathbf{e}_z z)} \mathbf{a}_E \quad \text{and} \quad \mathbf{H}_t(\Psi_t) = \frac{E_0}{\eta} e^{jk\mathbf{a}_t \cdot (\mathbf{e}_x x + \mathbf{e}_y y + \mathbf{e}_z z)} \mathbf{a}_H, \quad (2)$$

where E_0 is the magnitude of the incident electric field, $\mathbf{a} \cdot \mathbf{b}$ denotes the inner product of vectors \mathbf{a} and \mathbf{b} , $\eta = \sqrt{\frac{\mu}{\epsilon}}$ is the characteristic impedance, μ is the magnetic permeability, and ϵ is the electric permittivity. Moreover, \mathbf{e}_x , \mathbf{e}_y , and \mathbf{e}_z denote the unit vectors in the x , y , and z directions, respectively, and \mathbf{a}_E , \mathbf{a}_H , and \mathbf{a}_t denote the directions of the electric field, the magnetic field, and the propagation of the incident wave, which are all mutually orthogonal. In spherical coordinates, the incident direction

¹The polarization of the reflected wave with respect to the orientation of the receive antenna determines the amount of received power induced at a receiver. However, since the orientations of the receivers are random, the power loss due to the mismatch between the receive antenna orientation and the reflected wave polarization can be absorbed into the IRS-to-receiver channel gains. Hence, the polarization of the reflected wave is not explicitly included in Ψ_r , although it can be derived from our analysis, see Appendix A.

²In [21], the incident wave is always assumed to be in the $y - z$ plane and the polarization is either transverse electric x (TE^x) or transverse magnetic x (TM^x) to facilitate the analysis. While these assumptions are without loss of generality when analyzing one impinging wave, in this paper, we deal with scenarios where multiple waves may arrive from different angles and with different polarizations, and hence, these simplifying assumptions cannot simultaneously hold for all impinging waves. Therefore, we generalize the formulation of the electric and magnetic fields in [21] to arbitrary incident angles.

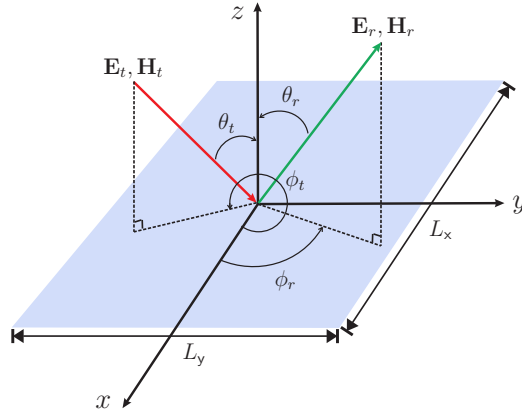


Fig. 2. Uniform plane wave impinges on a rectangular conducting tile with incident angle $\Psi_t = (\theta_t, \phi_t, \varphi_t)$ and is reflected with a desired reflection angle $\Psi_r = (\theta_r, \phi_r)$.

is defined as

$$\mathbf{a}_t = (\sin(\theta_t) \cos(\phi_t), \sin(\theta_t) \sin(\phi_t), \cos(\theta_t)) \triangleq (A_x(\Psi_t), A_y(\Psi_t), A_z(\Psi_t)). \quad (3)$$

Note that \mathbf{a}_E and \mathbf{a}_H lie in the plane orthogonal to \mathbf{a}_t . Let (H_x, H_y) denote the components of the magnetic field in the $x - y$ plane. Defining $\varphi_t = \tan^{-1}(\frac{H_y}{H_x})$, which determines the polarization of the wave, we obtain \mathbf{a}_E and \mathbf{a}_H as

$$\mathbf{a}_E = \mathbf{a}_H \times \mathbf{a}_t \quad \text{and} \quad \mathbf{a}_H = b(c(\Psi_t) \cos(\varphi_t), c(\Psi_t) \sin(\varphi_t), \sqrt{1 - c^2(\Psi_t)}), \quad (4)$$

where $c(\Psi_t) = \frac{A_z(\Psi_t)}{\sqrt{A_{x,y}^2(\Psi_t) + A_z^2(\Psi_t)}}$, $A_{x,y}(\Psi_t) = \cos(\varphi_t)A_x(\Psi_t) + \sin(\varphi_t)A_y(\Psi_t)$, $b = \text{sign}(\frac{H_x}{c(\Psi_t) \cos(\varphi_t)})$, $\text{sign}(\cdot)$ denotes the sign of a real number, and $\mathbf{a} \times \mathbf{b}$ denotes the cross product between vectors \mathbf{a} and \mathbf{b} . Note that the reference complex amplitude of the incident electric field in (1) can be obtained from the electric vector field in (2) as $E_t(\Psi_t) = E_0 e^{jk\mathbf{a}_t \cdot (\mathbf{e}_x x + \mathbf{e}_y y + \mathbf{e}_z z)}|_{(x,y,z)=(0,0,0)} = E_0$.

We assume that the surface impedance is suitably designed to realize reflection coefficient $\Gamma = \rho_{\text{eff}} e^{j\beta(x,y)}$, where $\beta(x,y)$ is the phase shift applied at point (x,y) on the tile and $\rho_{\text{eff}} \in (0, 1]$ is the efficiency factor of the tile which accounts for potential power losses [28], [29]³. Therefore, the tangential components of the scattered electric and magnetic fields are given by $\mathbf{E}_r = \Gamma \mathbf{E}_t$ and $\mathbf{H}_r = -\Gamma \mathbf{H}_t$, respectively. In order to determine the scattered fields, we employ the Electromagnetic Equivalence Theorem [21, Ch. 7] and assume that *only* scattered fields $(\mathbf{E}_r, \mathbf{H}_r)$ exist in the environment and that the IRS is replaced by a perfectly magnetically conducting (PMC) surface. To compensate for

³The induced current in (5) can be realized by a *locally* passive surface that is strictly lossy $\rho_{\text{eff}} < 1$ [29]. The current in (5) can also be generated by a loss-less surface that is *non-locally* passive (i.e., not all points on the surface may be passive, but the average power consumption across the entire surface is zero), see [28], [29] for detailed discussions.

the field discontinuity across the boundaries, an electric current $\mathbf{J}_r^{\text{pmc}} = \mathbf{n} \times \mathbf{H}_r|_{z=0}$ should be introduced on the surface, where \mathbf{n} is the normal vector of the surface [21, Ch. 7, eq. (7.42)]. Next, using the Image Theory for large flat surfaces [21, Ch. 7.4], an equivalent *obstacle-free* system is obtained by removing the PMC and replacing $\mathbf{J}_r^{\text{pmc}}$ with an equivalent electric current \mathbf{J}_r obtained as [21, Ch. 7.4, 7.8]

$$\begin{aligned} \mathbf{J}_r &= 2\mathbf{J}_r^{\text{pmc}} = 2\mathbf{n} \times \mathbf{H}_r|_{z=0} = -2\Gamma\mathbf{n} \times \mathbf{H}_t|_{z=0} \\ &\stackrel{(a)}{=} -2\rho_{\text{eff}} \frac{E_0}{\eta} e^{jk[A_x(\Psi_t)x + A_y(\Psi_t)y] + j\beta(x,y)} \mathbf{e}_z \times \mathbf{a}_H \stackrel{(b)}{=} e^{jk[A_x(\Psi_t)x + A_y(\Psi_t)y] + j\beta(x,y)} (J_x \mathbf{e}_x + J_y \mathbf{e}_y), \end{aligned} \quad (5)$$

where equality (a) follows from the assumption that the incident EM wave is a plane wave, and for equality (b), we used the definitions $J_x = 2\frac{E_0}{\eta} \rho_{\text{eff}} c(\Psi_t) \sin(\varphi_t)$ and $J_y = -2\frac{E_0}{\eta} \rho_{\text{eff}} c(\Psi_t) \cos(\varphi_t)$. The magnitude of the equivalent electric current is given by $\|\mathbf{J}_r\| = \sqrt{J_x^2 + J_y^2} = 2\rho_{\text{eff}} \frac{E_0}{\eta} c(\Psi_t)$, where depending on the incident angle and the polarization, we have $c(\Psi_t) \in [\cos(\theta_t), 1]$.

The reflected electric and magnetic fields induced by electric current \mathbf{J}_r in an obstacle-free environment are found as follows [21, Ch. 6]

$$\mathbf{E}_r = \frac{1}{j\omega\epsilon} \nabla \times \mathbf{H}_r \quad \text{and} \quad \mathbf{H}_r = \frac{1}{\mu} \nabla \times \mathbf{V}, \quad (6)$$

where $\nabla \times$ is the curl operator, $\omega = k/\sqrt{\mu\epsilon}$, and \mathbf{V} is an auxiliary vector potential, which assuming a far-field scenario is given by

$$\mathbf{V}(\Psi_r) = \frac{\mu e^{-jk\rho_r}}{4\pi\rho_r} \int_{x=-L_x/2}^{L_x/2} \int_{y=-L_y/2}^{L_y/2} \mathbf{J}_r(x, y) e^{jk\sqrt{x^2+y^2} \cos(\alpha)} dx dy. \quad (7)$$

Here, α is the angle between the vector specified by angle Ψ_r and the line that connects (x, y) with the origin.

In order to solve the integral equation in (7), we have to assume a given phase-shift profile, $\beta(x, y)$, for the tile surface, i.e., a transmission mode. One criterion to design a tile transmission mode is to facilitate reflection in a certain direction, i.e., the generalized Snell's law [4], [5]. In particular, we design the tile to reflect an EM wave impinging from direction Ψ_t^* towards direction Ψ_r^* and analyze the tile response function $g(\Psi_t, \Psi_r)$ caused by the corresponding phase-shift profile for an EM wave impinging from an arbitrary direction Ψ_t (including Ψ_t^*) and observed at an arbitrary observation angle Ψ_r (including Ψ_r^*). For ease of presentation, let us define the amplitude and phase of $g(\Psi_t, \Psi_r)$ as $g_{||}(\Psi_t, \Psi_r)$ and $g_{\angle}(\Psi_t, \Psi_r)$, respectively, up to a sign, i.e., $g_{||}(\Psi_t, \Psi_r) = \pm |g(\Psi_t, \Psi_r)|$ and $g_{\angle}(\Psi_t, \Psi_r) = \angle g(\Psi_t, \Psi_r) \pm \pi$ such that $g(\Psi_t, \Psi_r) = g_{||}(\Psi_t, \Psi_r) e^{jg_{\angle}(\Psi_t, \Psi_r)}$. Here, $|\cdot|$ and \angle denote the absolute value and phase

of a complex number. Moreover, let $A_i(\Psi_t, \Psi_r) = A_i(\Psi_t) + A_i(\Psi_r)$, $i \in \{x, y\}$.

Proposition 1: For given Ψ_t^* and Ψ_r^* , let us impose the following linear phase-shift function $\beta(x, y) = \beta(x) + \beta(y)$ with

$$\beta(x) = -kA_x(\Psi_t^*, \Psi_r^*)x + \frac{\beta_0}{2} \quad \text{and} \quad \beta(y) = -kA_y(\Psi_t^*, \Psi_r^*)y + \frac{\beta_0}{2}. \quad (8)$$

Then, the amplitude of the corresponding tile response function for an EM wave impinging from an arbitrary direction Ψ_t and observed at arbitrary reflection direction Ψ_r is obtained as

$$g_{||}^c(\Psi_t, \Psi_r) = \frac{\sqrt{4\pi}\rho_{\text{eff}}L_xL_y}{\lambda}\tilde{g}(\Psi_t, \Psi_r) \times \text{sinc}\left(\frac{kL_x[A_x(\Psi_t, \Psi_r) - A_x(\Psi_t^*, \Psi_r^*)]}{2}\right) \text{sinc}\left(\frac{kL_y[A_y(\Psi_t, \Psi_r) - A_y(\Psi_t^*, \Psi_r^*)]}{2}\right), \quad (9)$$

where $\text{sinc}(x) = \sin(x)/x$ and

$$\tilde{g}(\Psi_t, \Psi_r) = c(\Psi_t) \left\| \left[\begin{array}{c} \cos(\varphi_t) \cos(\theta_r) \sin(\phi_r) - \sin(\varphi_t) \cos(\theta_r) \cos(\phi_r) \\ \sin(\varphi_t) \sin(\phi_r) + \cos(\varphi_t) \cos(\phi_r) \end{array} \right] \right\|_2. \quad (10)$$

The phase of the tile response function is obtained as $g_Z^c(\Psi_t, \Psi_r) = \frac{\pi}{2} + \beta_0$.

Proof: The proof is provided in Appendix A. ■

Corollary 1: Assuming large $L_x, L_y \gg \lambda$ and $\Psi_t^* = \Psi_t$, the maximum value of $|g(\Psi_t, \Psi_r)|$ is observed at $\Psi_r = \Psi_r^*$ and is given by

$$\lim_{\Psi_r \rightarrow \Psi_r^*} |g^c(\Psi_t, \Psi_r)| = \frac{\sqrt{4\pi}\rho_{\text{eff}}L_xL_y}{\lambda}\tilde{g}(\Psi_t^*, \Psi_r^*) \stackrel{(a)}{\leq} \frac{\sqrt{4\pi}\rho_{\text{eff}}L_xL_y}{\lambda}, \quad (11)$$

where (a) holds with equality for incident and reflection directions normal to the surface, $\theta_t = \theta_r = 0$.

Proof: For $L_x, L_y \gg \lambda$, the sinc functions in (9) decay fast when $|A_i(\Psi_t, \Psi_r) - A_i(\Psi_t^*, \Psi_r^*)| > 0$, $i \in \{x, y\}$, whereas $\tilde{g}(\Psi_t, \Psi_r) \neq 0$, $\forall \Psi_t, \Psi_r$, is not a function of L_x, L_y and does not vary as quickly as the sinc functions. Hence, $|g^c(\Psi_t, \Psi_r)|$ attains its maximum value when the sinc functions have their maximum values, i.e., $A_i(\Psi_t, \Psi_r) = A_i(\Psi_t^*, \Psi_r^*)$ or equivalently at $\Psi_r = \Psi_r^*$ for $\Psi_t^* = \Psi_t$. Moreover, for normal incident, we have $c(\Psi_t) = 1$ and for normal reflection, the norm term in (10) is one. This implies that $\tilde{g}(\Psi_t^*, \Psi_r^*)$ attains its maximum value, i.e., one, which leads to the inequality in (11). ■

Proposition 1 reveals the impact of different system parameters on the tile response function $g^c(\Psi_t, \Psi_r)$. Fig. 3 shows the amplitude of the tile response function for both specular and anomalous reflections for several tile sizes. We now highlight some insights from Proposition 1 and Fig. 3:

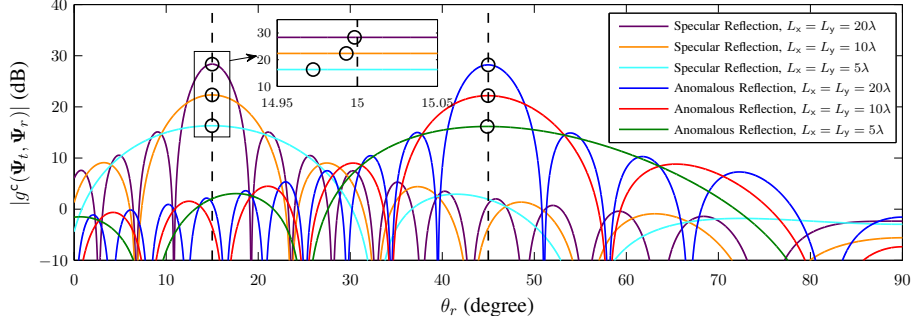


Fig. 3. Amplitude of response function, $|g^c(\Psi_t, \Psi_r)|$, in dB vs. θ_r for an $L_x \times L_y$ continuous tile, $(\theta_t, \phi_t, \varphi_t) = (15^\circ, 225^\circ, 22.5^\circ)$, $\phi_r = 45^\circ$, and $\rho_{\text{eff}} = 0.5$. We assume $(\theta_t^*, \phi_t^*) = (15^\circ, 225^\circ)$ and $(\theta_r^*, \phi_r^*) = (15^\circ, 45^\circ)$ for specular reflection and $(\theta_t^*, \phi_t^*) = (15^\circ, 225^\circ)$ and $(\theta_r^*, \phi_r^*) = (45^\circ, 45^\circ)$ for anomalous reflection.

i) Eq. (9) and Fig. 3 show that $|g^c(\Psi_t, \Psi_r)|$ becomes narrower as L_x and L_y increase. However, even for large tiles of size $L_x = L_y = 20\lambda$, the 10-dB beamwidth⁴ is around 6 degree which can cause significant interference to unintended receivers in far-field scenarios.

ii) Fig. 3 suggests that for a given tile size, the peak and beamwidth of $|g^c(\Psi_t, \Psi_r)|$ for anomalous reflection are in general different from those for specular reflection.

iii) Let $\Psi_r^* = \text{argmax}_{\Psi_r} |g^c(\Psi_t, \Psi_r)|$. One expects to obtain $\Psi_r^* = (\theta_t, \pi + \phi_t) = \Psi_r^*$ for specular reflection; however, this is generally not true, see also [21, p. 596]. The reason for this behavior is that although the sinc functions in (9) attain their maximum values at $\Psi_r = \Psi_r^*$, this is not necessarily the case for $\tilde{g}(\Psi_t, \Psi_r)$ which can cause Ψ_r^* to deviate from Ψ_r^* . For instance, Fig. 3 shows that for $L_x = L_y = 5\lambda$, the maximum value of $|g^c(\Psi_t, \Psi_r)|$ occurs at $\theta_r = 14.97^\circ$ instead of at $\theta_r^* = \theta_t = 15^\circ$. Nevertheless, for large $L_x, L_y \gg \lambda$, the width of the sinc functions decreases and eventually they become the dominant factors for determining Ψ_r^* which yields $\Psi_r^* = \Psi_r^*$, cf. Corollary 1.

iv) For the phase-shift function in (8), the phase of $g^c(\Psi_t, \Psi_r)$ is equal to β_0 up to a constant. In other words, if we change the phase induced on the *entire tile surface* by a constant, $|g^c(\Psi_t, \Psi_r)|$ remains the same and $\angle g^c(\Psi_t, \Psi_r)$ changes by that constant.

Remark 1: The result given in [16, Lemma 2] is a special case of Proposition 1 with $\phi_t = \frac{3\pi}{2}$, $\varphi_t = \frac{\pi}{2}$, $\phi_r^* = \phi_r = \frac{\pi}{2}$, $\rho_{\text{eff}} = 1$, and $A_i(\Psi_t^*, \Psi_r^*) = \beta_0 = 0$, $i \in \{x, y\}$, which implies $\tilde{g}(\Psi_t, \Psi_r) = c(\Psi_t) = \cos(\theta_t)$, $A_x(\Psi_t, \Psi_r) = 0$ and $A_y(\Psi_t, \Psi_r) = \sin(\theta_r) - \sin(\theta_t)$.

C. Discrete Tiles

Although Proposition 1 provides insights regarding the impact of the system parameters, a continuous programmable tile surface is difficult to implement and, in practice, each tile is comprised of many

⁴Here, the 10-dB beamwidth is defined as the maximum range of θ_r around θ_r^* for which $|g(\Psi_t, \Psi_r)|$ is not more than 10 dB smaller than its maximum value.

discrete sub-wavelength unit cells, see Fig. 1. Therefore, let us now assume that each tile consists of $Q_x Q_y$ unit cells of size $L_e \times L_e$ which are uniformly spaced along the x and y axes with a spacing of d_x and d_y , respectively. For simplicity, we assume Q_x and Q_y are even numbers. Therefore, the position of the (n_x, n_y) -th unit cell is given by $(x, y) = (n_x d_x, n_y d_y)$ for $n_x = -\frac{Q_x}{2} + 1, \dots, \frac{Q_x}{2}$ and $n_y = -\frac{Q_y}{2} + 1, \dots, \frac{Q_y}{2}$. Moreover, we assume that the (n_x, n_y) -th unit cell applies a phase shift β_{n_x, n_y} to the reflected electric field. Exploiting Proposition 1, assuming $L_e \ll \lambda$, and using the identity $\lim_{x \rightarrow 0} \text{sinc}(x) = 1$, we can characterize the response of an individual unit cell, denoted by $g_{n_x, n_y}(\Psi_t, \Psi_r)$, $\forall n_x, n_y$, as

$$g_{n_x, n_y}(\Psi_t, \Psi_r) = \frac{j\sqrt{4\pi}\rho_{\text{eff}}L_e^2}{\lambda} \tilde{g}(\Psi_t, \Psi_r) e^{jk d_x [A_x(\Psi_t) + A_x(\Psi_r)] n_x} e^{jk d_y [A_y(\Psi_t) + A_y(\Psi_r)] n_y} e^{j\beta_{n_x, n_y}}, \quad (12)$$

The tile response function, denoted by $g^d(\Psi_t, \Psi_r)$, of the entire tile is the superposition of the fields generated by all its unit cells [30, Ch. 3] and is obtained as

$$g^d(\Psi_t, \Psi_r) = \sum_{n_x = -\frac{Q_x}{2} + 1}^{\frac{Q_x}{2}} \sum_{n_y = -\frac{Q_y}{2} + 1}^{\frac{Q_y}{2}} g_{n_x, n_y}(\Psi_t, \Psi_r). \quad (13)$$

The following proposition presents the phase-shift design needed to realize the generalized Snell's law and the resulting tile response function. For future reference, let us define $S_e(\Psi_t, \Psi_r) = \frac{j\sqrt{4\pi}\rho_{\text{eff}}L_e^2}{\lambda} \times \tilde{g}(\Psi_t, \Psi_r)$ as the unit cell factor which depends on the polarization of the incident wave, the incident angle Ψ_t , the size of each unit cell, and the observation angle Ψ_r [21].

Proposition 2: For given Ψ_t^* and Ψ_r^* , let us impose the constant phase shifts $\beta_{n_x, n_y} = \beta_{n_x} + \beta_{n_y}$ with

$$\beta_{n_x} = -k d_x A_x(\Psi_t^*, \Psi_r^*) n_x + \frac{\beta_0}{2} \quad \text{and} \quad \beta_{n_y} = -k d_y A_y(\Psi_t^*, \Psi_r^*) n_y + \frac{\beta_0}{2}. \quad (14)$$

Then, the amplitude of the corresponding tile response function for an EM wave impinging from an arbitrary direction Ψ_t and being observed at arbitrary reflection direction Ψ_r is given by

$$g_{\parallel}^d(\Psi_t, \Psi_r) = |S_e(\Psi_t, \Psi_r)| \times \frac{\sin\left(\frac{\pi Q_x d_x}{\lambda} [A_x(\Psi_t, \Psi_r) - A_x(\Psi_t^*, \Psi_r^*)]\right)}{\sin\left(\frac{\pi d_x}{\lambda} [A_x(\Psi_t, \Psi_r) - A_x(\Psi_t^*, \Psi_r^*)]\right)} \times \frac{\sin\left(\frac{\pi Q_y d_y}{\lambda} [A_y(\Psi_t, \Psi_r) - A_y(\Psi_t^*, \Psi_r^*)]\right)}{\sin\left(\frac{\pi d_y}{\lambda} [A_y(\Psi_t, \Psi_r) - A_y(\Psi_t^*, \Psi_r^*)]\right)} \quad (15)$$

and the phase of the tile response function is given by

$$g_{\perp}^d(\Psi_t, \Psi_r) = \beta_0 + \frac{\pi}{2} + \frac{\pi d_x [A_x(\Psi_t, \Psi_r) - A_x(\Psi_t^*, \Psi_r^*)]}{\lambda} + \frac{\pi d_y [A_y(\Psi_t, \Psi_r) - A_y(\Psi_t^*, \Psi_r^*)]}{\lambda}. \quad (16)$$

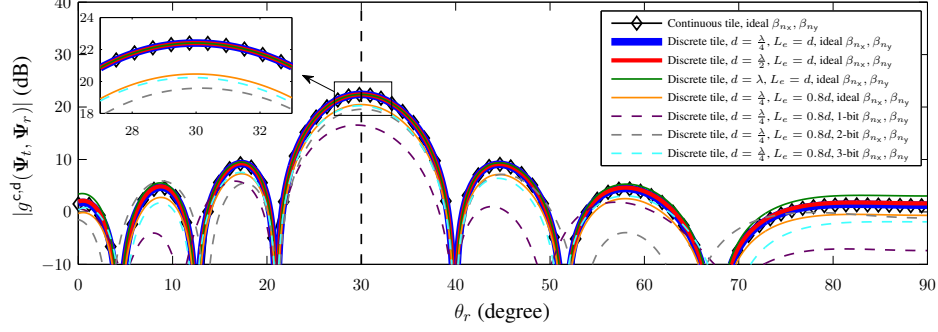


Fig. 4. Amplitude of the tile response function, $|g^{c,d}(\Psi_t, \Psi_r)|$, in dB vs. θ_r for $(\theta_t, \phi_t, \varphi_t) = (0, 0, 22.5^\circ)$, $\phi_r = 45^\circ$, $(\theta_t^*, \phi_t^*) = (0, 0)$, $(\theta_r^*, \phi_r^*) = (30^\circ, 45^\circ)$, $d_x = d_y = d$, and $\rho_{\text{eff}} = 0.5$. For a fair comparison, the sizes of the continuous and discrete tiles are identical with $L_x = L_y = 10\lambda$. For discrete tiles, the number of unit cells along the x and y axes are $Q_x = \frac{L_x}{d_x}$ and $Q_y = \frac{L_y}{d_y}$, respectively, the unit cell size is $L_e \times L_e$, and we consider both ideal continuous and uniformly quantized phase shifts β_{n_x} and β_{n_y} .

Proof: The proof is given in Appendix B. ■

Corollary 2: Assuming large Q_x and Q_y , $d_x, d_y \ll \lambda$, and $\Psi_t^* = \Psi_t$, the maximum value of $|g^d(\Psi_t, \Psi_r)|$ occurs at $\Psi_r = \Psi_r^*$ and is obtained as

$$\lim_{\Psi_r \rightarrow \Psi_r^*} |g^d(\Psi_t, \Psi_r)| = |S_e(\Psi_t^*, \Psi_r^*)| Q_x Q_y \stackrel{(a)}{\leq} \frac{\sqrt{4\pi} \rho_{\text{eff}} L_e^2}{\lambda} Q_x Q_y, \quad (17)$$

where (a) holds with equality for incident and reflection directions normal to the surface, $\theta_t = \theta_r = 0$.

Proof: The proof is similar to the proof for Corollary 1. ■

In Fig. 4, we plot $|g^d(\Psi_t, \Psi_r)|$ obtained from Proposition 2 vs. θ_r for various scenarios and compare it with $|g^c(\Psi_t, \Psi_r)|$ obtained from Proposition 1. In the following, we highlight some insights that Proposition 2 and Fig. 4 provide:

i) For $d_x, d_y \rightarrow 0$ (extremely sub-wavelength unit cells) and $L_e = d_x = d_y$ (compact deployment of the unit cells), the tile response function of a discrete tile in Proposition 2 becomes identical to that of a continuous tile in Proposition 1, i.e., $g^d(\Psi_t, \Psi_r) = g^c(\Psi_t, \Psi_r)$.

ii) Fig. 4 shows that for a discrete tile to accurately approximate a continuous tile, it is sufficient that $L_e = d_x = d_y \leq \frac{\lambda}{2}$ holds. In practice, there are gaps between the IRS unit cells, i.e., $L_e < d_x, d_y$. This leads to a decrease of the effective size of the tile, see Fig. 4 for $L_e = 0.8d$.

iii) In both Propositions 1 and 2, we assumed that the phase shift introduced by the tile unit cells can assume any real value which is an idealized assumption as finite resolution phase shifts are typically applied in practice. Nevertheless, Fig. 4 suggests that a 3-bit uniform quantization of the phase shifts β_{n_x} and β_{n_y} yields a tile response function which is very close to the one obtained for ideal real-valued phase shifts. Moreover, from Fig. 4, we also observe that even for a 1-bit phase shift quantization, the tile response function has a shape similar to the ideal case although the peak is reduced and the side

lobes deviate from the ideal real-valued phase shifts, which is consistent with [4].

D. End-to-End Channel Model

Using the tile response function $|g(\Psi_t, \Psi_r)|$ derived in the previous sections, we now develop an end-to-end channel model for IRS-assisted wireless systems comprising multiple transmitters and multiple receivers. In particular, we consider a general system comprising N_t multiple-antenna transmitters, an IRS, and N_r multiple-antenna receivers. In addition, we assume there are multiple scatterers in the environment which cause the signal of a given transmitter to arrive at the IRS potentially via multiple paths and the signal reflected from the IRS to potentially also arrive at a given receiver via multiple paths [31], [32]. The resulting end-to-end channel model can be compactly written as follows

$$\mathbf{y}^{(j)} = \sum_{i=1}^{N_t} \left[\underbrace{b_d^{(j,i)} \mathbf{A}_d^{(j,i)} \boldsymbol{\Sigma}_d^{(j,i)} \mathbf{D}_d^{(j,i)H}}_{\text{direct paths}} + \underbrace{b_r^{(j)} b_t^{(i)} \mathbf{A}_r^{(j)} \boldsymbol{\Sigma}_r^{(j)} \mathbf{G}^{(j,i)} \boldsymbol{\Sigma}_t^{(i)} \mathbf{D}_t^{(i)H}}_{\text{IRS-guided paths}} \right] \mathbf{x}^{(i)} + \mathbf{z}^{(j)}, \quad j = 1, \dots, N_r, \quad (18)$$

where $(\cdot)^H$ denotes the Hermitian operator, $\mathbf{x}^{(i)} \in \mathbb{C}^{T_i}$ is the transmit symbol vector of the i -th transmitter which is equipped with T_i transmit antennas; $\mathbf{y}^{(j)} \in \mathbb{C}^{J_j}$ denotes the receive vector at the j -th receiver which is equipped with J_j receive antennas; and $\mathbf{z}^{(j)} \in \mathbb{C}^{J_j}$ denotes the additive white Gaussian noise (AWGN) at the j -th receiver. Here, \mathbb{C} denotes the set of complex numbers. Moreover, $b_d^{(j,i)}$, $b_t^{(i)}$, $b_r^{(j)} \in \{0, 1\}$ are binary variables modeling the potential blockage of the transmitter i -to-receiver j , transmitter i -to-IRS, and IRS-to-receiver j links, respectively. Furthermore, $\mathbf{A}_r^{(j)} \in \mathbb{C}^{J_j \times L_r^{(j)}}$ and $\mathbf{D}_t^{(i)} \in \mathbb{C}^{T_i \times L_t^{(i)}}$ ($\mathbf{A}_d^{(j,i)} \in \mathbb{C}^{J_j \times L_d^{(j,i)}}$ and $\mathbf{D}_d^{(j,i)} \in \mathbb{C}^{T_i \times L_d^{(j,i)}}$) are matrices whose columns are the receive and transmit steering vectors evaluated at the angles-of-arrival (AoAs) and angles-of-departure (AoDs) of the IRS-assisted paths (direct paths), respectively, where $L_d^{(j,i)}$, $L_t^{(i)}$, and $L_r^{(j)}$ denote the numbers of scatterers for the transmitter i -to-receiver j , transmitter i -to-IRS, and IRS-to-receiver j links, respectively. Furthermore, $\boldsymbol{\Sigma}_d^{(j,i)} \in \mathbb{C}^{L_d^{(j,i)} \times L_d^{(j,i)}}$, $\boldsymbol{\Sigma}_t^{(i)} \in \mathbb{C}^{L_t^{(i)} \times L_t^{(i)}}$, and $\boldsymbol{\Sigma}_r^{(j)} \in \mathbb{C}^{L_r^{(j)} \times L_r^{(j)}}$ are diagonal matrices containing the channel coefficients of the transmitter i -to-receiver j , transmitter i -to-IRS, and IRS-to-receiver j paths, respectively. Note that $\boldsymbol{\Sigma}_d^{(j,i)}$, $\boldsymbol{\Sigma}_t^{(i)}$, and $\boldsymbol{\Sigma}_r^{(j)}$ contain the impact of path-loss as well as small-scale and large-scale fading. Finally, matrix $\mathbf{G}^{(j,i)} \in \mathbb{C}^{L_r^{(j)} \times L_t^{(i)}}$ contains the tile response functions evaluated for the respective AoAs and AoDs at the IRS as explained in the following.

We assume that the IRS can select for each tile one of the possible transmission modes corresponding to one phase-shift function $\beta(x, y)$ in Proposition 1 or one set of unit cell phase shifts $\beta_{n_x, n_y}, \forall n_x, n_y$, in Proposition 2. The design of a finite number of transmission modes, M , will be discussed in detail in

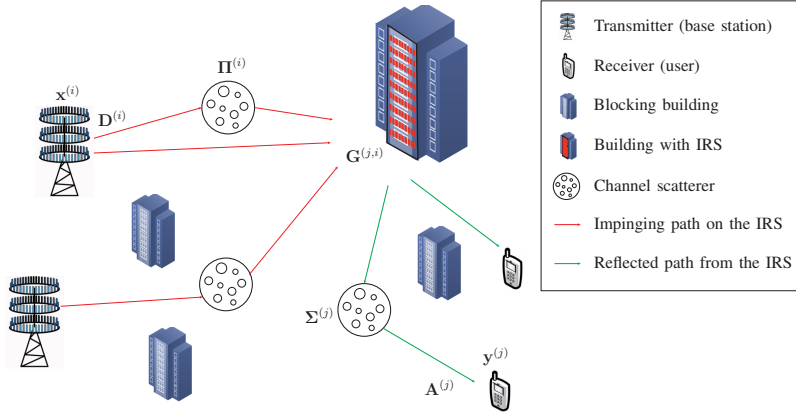


Fig. 5. Schematic illustration of an IRS-assisted wireless system. Only the IRS-guided paths are shown for clarity of presentation.

Section III-A. Let $s_{n,m} \in \{0, 1\}$ denote a binary variable which is equal to one if the m -th transmission mode is selected for the n -th tile; otherwise, it is equal to zero. Moreover, let $\mathcal{M} \subset \{1, \dots, M\}$ denote the subset of transmission modes that is used for resource allocation in a given frame. We will discuss the design of \mathcal{M} in Section III-A. Since, at any given time, the IRS can select only one transmission mode for each tile, $\sum_{m \in \mathcal{M}} s_{n,m} = 1, \forall n$, has to hold. Then, matrix $\mathbf{G}^{(j,i)}$ can be expressed as

$$\mathbf{G}^{(j,i)} = \sum_{n=1}^N \sum_{m \in \mathcal{M}} s_{n,m} \mathbf{G}_{n,m}^{(j,i)} \quad \text{with} \quad [\mathbf{G}_{n,m}^{(j,i)}]_{n_r, n_t} = g_{n,m}(\Psi_t^{(n_t)}, \Psi_r^{(n_r)}). \quad (19)$$

Here, $g_{n,m}(\Psi_t^{(n_t)}, \Psi_r^{(n_r)})$ denotes the response function of the n -th tile for the m -th transmission mode evaluated at the n_t -th AoA, specified by angle $\Psi_t^{(n_t)}$, and the n_r -th AoD, specified by angle $\Psi_r^{(n_r)}$. Assuming that the center of the n -th tile is placed at point $(x, y) = (K_x^{(n)} L_x, K_y^{(n)} L_y)$, where $K_x^{(n)}$ and $K_y^{(n)}$ are integer numbers, $g_{n,m}(\Psi_t, \Psi_r)$ for AoA Ψ_t and AoD Ψ_r can be expressed as

$$g_{n,m}(\Psi_t, \Psi_r) = e^{jkK_x^{(n)} L_x A_x(\Psi_t, \Psi_r) + jkK_y^{(n)} L_y A_y(\Psi_t, \Psi_r)} g_m(\Psi_t, \Psi_r), \quad (20)$$

where $g_m(\Psi_t, \Psi_r)$ is the response function of the reference tile centered at the origin with $K_x^{(n)} = K_y^{(n)} = 0$, which is given in Propositions 1 and 2.

Defining $\mathbf{H}_1^{(i)} = b_t^{(i)} \Sigma_t^{(i)} \mathbf{D}_t^{(i)}$, $\mathbf{H}_2^{(j)} = b_r^{(j)} \mathbf{A}_r^{(j)} \Sigma_r^{(j)}$, and $\mathbf{H}_d^{(j,i)} = b_d^{(j,i)} \mathbf{A}_d^{(j)} \Sigma_d^{(j,i)} \mathbf{D}_d^{(i)}$, the channel model in (18) can be rewritten as follows

$$\mathbf{y}^{(j)} = \sum_{i=1}^{N_t} \left[\mathbf{H}_d^{(j,i)} + \sum_{n=1}^N \sum_{m \in \mathcal{M}} s_{n,m} \mathbf{H}_{n,m}^{(j,i)} \right] \mathbf{x}^{(i)} + \mathbf{z}^{(j)}, \quad j = 1, \dots, N_r, \quad (21)$$

where $\mathbf{H}_{n,m}^{(j,i)} = \mathbf{H}_2^{(j)} \mathbf{G}_{n,m}^{(j,i)} \mathbf{H}_1^{(i)}$ denotes the end-to-end channel for the n -th tile assuming it is programmed as an anomalous reflector to enable the m -th transmission mode. Furthermore, defining $\mathbf{H}_{e2e}^{(j,i)} = \mathbf{H}_d^{(j,i)} +$

$\sum_{n=1}^N \sum_{m \in \mathcal{M}} s_{n,m} \mathbf{H}_{n,m}^{(j,i)}$ as the effective IRS-assisted end-to-end channel between transmitter i and receiver j , the channel model in (21) explicitly shows that unlike conventional systems, for which the channel matrix is fixed, for IRS-assisted communications, we can choose among $|\mathcal{M}|^N$ different end-to-end channel matrices which implies the realization of a smart reconfigurable wireless environment [2], [3].

Remark 2: Let P_r be the power received at the receiver. Using (1) and Proposition 2, we have

$$\sqrt{\frac{P_r|_{\text{IRS}}}{P_r|_{\text{direct}}}} \propto \frac{\frac{1}{\sqrt{4\pi\rho_t}} \times Ng \times \frac{1}{\sqrt{4\pi\rho_r}}}{\frac{1}{\sqrt{4\pi\rho_d}}} \stackrel{(a)}{\propto} \frac{\lambda\rho_d}{4\rho_t\rho_r} \times NQ_x Q_y, \quad (22)$$

where for (a), we replaced the tile response g with its maximum value $\frac{\sqrt{\pi}\lambda}{2} Q_x Q_y$ from Corollary 2 for $L_e = \frac{\lambda}{2}$ and $\rho_{\text{eff}} = 1$. We observe from (22) that the number of IRS unit cells required for the IRS-assisted link to have a similar strength as the unobstructed direct link scales as $Q = NQ_x Q_y \propto \frac{4\rho_t\rho_r}{\lambda\rho_d}$. Now, suppose that the IRS is deployed in the middle between the transmitter and receiver. In this case, for $(\rho_d, \rho_t, \rho_r) = (200 \text{ m}, 100 \text{ m}, 100 \text{ m})$ and carrier frequency 5 GHz, $Q = 3333$ unit cells are needed. On the other hand, if the IRS is deployed close to the receiver such that $(\rho_d, \rho_t, \rho_r) = (200 \text{ m}, 180 \text{ m}, 20 \text{ m})$, only $Q = 1200$ unit cells are needed. Hence, deploying the IRS close to the receivers (or transmitters) is advantageous, see [16]–[18] for similar arguments. We further study the impact of the position of the IRS on performance in Fig. 10 in Section IV.

III. TWO-STAGE OPTIMIZATION FRAMEWORK FOR IRS-ASSISTED COMMUNICATIONS

Based on the end-to-end model developed in Section II, in this section, we propose a two-stage framework for IRS optimization, namely an offline design stage and an online optimization stage.

A. Offline Tile Transmission Mode Codebook Design

In the following, we design a tile transmission mode codebook comprised of a finite number of predefined phase-shift configurations according to (8) in Proposition 1 or (14) in Proposition 2, i.e.,

$$\begin{cases} e^{j\beta(x,y)} = e^{-jkA_x(\Psi_t^*, \Psi_r^*)x} \times e^{-jkA_y(\Psi_t^*, \Psi_r^*)y} \times e^{j\beta_0}, & \text{continuous tile} \\ e^{j\beta_{n_x, n_y}} = e^{-jkd_x A_x(\Psi_t^*, \Psi_r^*)n_x} \times e^{-jkd_y A_y(\Psi_t^*, \Psi_r^*)n_y} \times e^{j\beta_0}, & \text{discrete tile.} \end{cases} \quad (23)$$

The above phase-shift profiles $\beta(x, y)$ and β_{n_x, n_y} are affine functions in variables (x, y) and (n_x, n_y) , respectively. Thereby, the slope of the phase-shift function determines the direction of the reflected wavefront and the affine constant β_0 determines the phase of the wavefront. In the following, instead

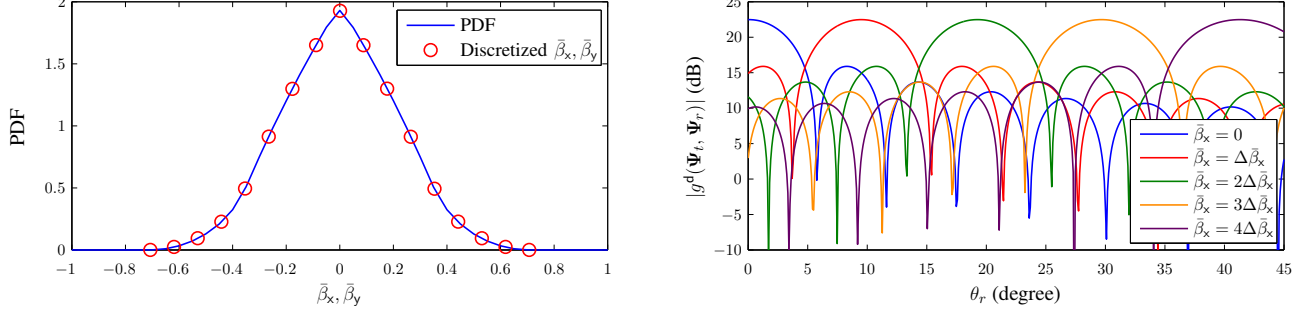


Fig. 6. *Left-hand side*: Distribution of $\bar{\beta}_x$ and $\bar{\beta}_y$ and discretized values with $\Delta\bar{\beta}_i = \frac{\sqrt{2}}{16}$ and $\bar{\beta}_i^{\max} = \frac{\sqrt{2}}{2}$, where elevation angles (θ_t^*, θ_r^*) (azimuth angles (ϕ_t^*, ϕ_r^*)) are uniformly distributed in interval $[0, \pi/4]$ ($[0, 2\pi]$), *Right-hand side*: $|g^d(\Psi_t, \Psi_r)|$ in dB vs. θ_r for $(\theta_t, \phi_t, \varphi_t) = (0, 0, 0)$, $\phi_r = 0$, $\bar{\beta}_y = 0$, $L_x = L_y = 10\lambda$, $d_x = d_y = L_e = \frac{\lambda}{2}$, and $\rho_{\text{eff}} = 0.5$.

of discretizing the expected angle of the incident EM wave, Ψ_t^* , and the desired angle of the reflected EM wave, Ψ_r^* , to construct the codebook, we directly discretize $A_i(\Psi_t^*, \Psi_r^*)$, $i \in \{x, y\}$. This is a more efficient design since different (Ψ_t^*, Ψ_r^*) may yield the same value of $A_i(\Psi_t^*, \Psi_r^*)$, $i \in \{x, y\}$. From (3), we have $A_i(\Psi_t^*, \Psi_r^*) \in [-2, 2]$. For notational convenience, let us define the following normalized variables $\bar{\beta}_i = A_i(\Psi_t^*, \Psi_r^*)/2$, $i \in \{x, y\}$, and $\bar{\beta}_0 = \beta_0/\pi$ such that $\bar{\beta}_i \in [-1, 1]$, $\forall i \in \{x, y, 0\}$. Therefore, we assume that the transmission mode codebook is the product of three component codebooks, namely $\bar{\beta}_x \in \mathcal{B}_x$, $\bar{\beta}_y \in \mathcal{B}_y$, and $\bar{\beta}_0 \in \mathcal{B}_0$, where \mathcal{B}_x and \mathcal{B}_y are referred to as the reflection codebooks and \mathcal{B}_0 is referred to as the wavefront phase codebook. Assuming that the size of the entire codebook is M , we have $M = |\mathcal{B}_x| \times |\mathcal{B}_y| \times |\mathcal{B}_0|$.

Reflection Codebooks: We assume all tiles use the same reflection codebook \mathcal{B}_i , $i \in \{x, y\}$. One simple option for construction of \mathcal{B}_i is the uniform discretization of $\bar{\beta}_i$, $i \in \{x, y\}$, i.e., $\mathcal{B}_i = \{0, \pm\Delta\bar{\beta}_i, \dots, \pm\bar{\beta}_i^{\max}\}$, where $\Delta\bar{\beta}_i = \frac{2\bar{\beta}_i^{\max}}{|\mathcal{B}_i|-1}$ and $\bar{\beta}_i^{\max} \in (0, 1]$ is the maximum range of parameter $\bar{\beta}_i$. In particular, $\bar{\beta}_i^{\max}$ may be chosen smaller than one if the EM waves impinging and reflected at the IRS exhibit a limited range of AoAs and AoDs, respectively. For example, the left-hand side of Fig. 6 shows the distribution of $\bar{\beta}_x$ and $\bar{\beta}_y$ when the elevation angles (θ_t^*, θ_r^*) (azimuth angles (ϕ_t^*, ϕ_r^*)) are uniformly distributed in the interval $[0, \pi/4]$ ($[0, 2\pi]$). In this case, from (3), it follows that $|\bar{\beta}_i| \leq \frac{\sqrt{2}}{2} \approx 0.7071$. Therefore, as an example codebook, we may adopt $\Delta\bar{\beta}_i = \frac{\sqrt{2}}{16}$ and $\bar{\beta}_i^{\max} = \frac{\sqrt{2}}{2}$ which leads to codebook $\mathcal{B}_x = \mathcal{B}_y = \{0, \pm\frac{\sqrt{2}}{16}, \pm\frac{\sqrt{2}}{8}, \dots, \pm\frac{\sqrt{2}}{2}\}$ of size seventeen. The right-hand side of Fig. 6 shows the amplitude of the tile response function $|g^d(\Psi_t, \Psi_r)|$ for the phase-shift configurations generated by $\bar{\beta}_x = 0, \frac{\sqrt{2}}{16}, \frac{\sqrt{2}}{8}, \frac{3\sqrt{2}}{16}, \frac{\sqrt{2}}{4}$ and $\bar{\beta}_y = 0$ when the incident wave is normal to the surface and the observation point lies in the $x - z$ plane, i.e., $(\theta_t, \phi_t, \varphi_t) = (0, 0, 0)$, $\phi_r = 0$. As can be observed from this figure, the resulting tile response functions cover the considered range of elevation angles for the reflected EM wave, i.e., $\theta_r \in [0, \pi/4]$.

Wavefront Phase Codebook: The role of $\bar{\beta}_0$ is to control the superposition of the waves reflected from different tiles at the receiver. In particular, if different tiles employ the same $\bar{\beta}_x$ and $\bar{\beta}_y$, they can cancel the phase differences caused by their different positions by choosing appropriate values for $\bar{\beta}_0$, see (20). In other words, for two tiles n and $n' \neq n$ to reflect an EM wave impinging from incident direction Ψ_t^* along reflection direction Ψ_r^* , they not only have to choose appropriate and *identical* elements from the reflection codebooks but also phase shifts, denoted by $\bar{\beta}_0^{(n)}$ and $\bar{\beta}_0^{(n')}$, respectively, that meet

$$\bar{\beta}_0^{(n)} - \bar{\beta}_0^{(n')} = \frac{1}{\pi} \text{mod} \left(-2k \left[(K_x^{(n)} - K_x^{(n')}) L_x \bar{\beta}_x^* + (K_y^{(n)} - K_y^{(n')}) L_y \bar{\beta}_y^* \right], 2\pi \right), \quad \forall n' \neq n, \quad (24)$$

where $\bar{\beta}_x^* = A_x(\Psi_t^*, \Psi_r^*)/2$, $\bar{\beta}_y^* = A_y(\Psi_t^*, \Psi_r^*)/2$, and $\text{mod}(x, y)$ denotes the y -modulus of real number x which is needed due to the periodicity of the complex exponential function in (23). Similar to the reflection codebooks, one simple option is to employ uniform discretization, i.e., $\mathcal{B}_0 = \{0, \pm\Delta\bar{\beta}_0, \dots, \pm\bar{\beta}_0^{\max}\}$, where $\Delta\bar{\beta}_0 = \frac{2\bar{\beta}_0^{\max}}{|\mathcal{B}_0|-1}$ and $\bar{\beta}_0^{\max} \leq 1$ is the maximum range of $\bar{\beta}_0$ which can be chosen strictly smaller than one if prior knowledge about the range of (Ψ_t^*, Ψ_r^*) is available.

B. Mode Pre-selection for Online Optimization

For the end-to-end channel model in (21), a given channel realization corresponds to a given number of scatterers in the environment. Therefore, due to the limited number of AoAs and AoDs pointing from the IRS to these scatterers, especially at high frequencies, only a limited number of phase-shift configurations in the reflection codebooks are suitable for reflecting the EM wave impinging from one of the scatterers/transmitters towards one of the other scatterers/receivers, see Fig. 5. In other words, for a given transmitter-receiver pair, the value of $\|\mathbf{H}_{n,m}^{(j,i)}\|_F$, where $\|\cdot\|_F$ denotes the Frobenius norm, is non-negligible only for a few of the transmission modes in the codebook. Therefore, before online optimization, we can first pre-select a subset of the possible transmission modes, whose indices are collected in set \mathcal{M} . The exact criterion for this pre-selection depends on the application, of course. For instance, one may determine \mathcal{M} based on the strength of the corresponding channel, i.e.,

$$\mathcal{M} = \{m | \exists(i, j, n) : \|\mathbf{H}_{n,m}^{(j,i)}\|_F \geq \delta\}, \quad (25)$$

where δ is a threshold parameter. Alternatively, one may consider more sophisticated criteria that account for the resulting interference at other users (e.g., for multi-user communications) or the information leakage to eavesdroppers (e.g., for secure communications).

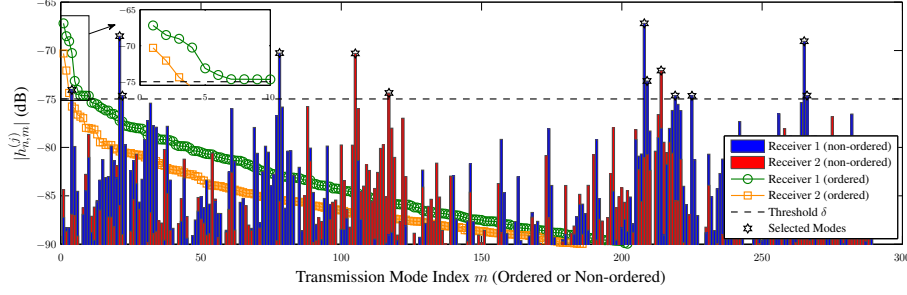


Fig. 7. Illustration of codebook size reduction for online optimization. Channel strength $|h_{n,m}^{(j)}|$ for one tile and one channel realization versus the transmission mode index. The same IRS parameters and reflection codebook as for Fig. 6 are assumed.

Fig. 7 shows an example for transmission mode selection for a system consisting of one single-antenna transmitter, an IRS, and two single-antenna receivers. The IRS parameters and the offline codebook are identical to those used in Fig. 6, i.e., the reflection codebooks have 17×17 elements. We assume that there exist two paths (e.g., the direct path and one path via a scatterer) for each of the transmitter-to-IRS and IRS-to-receiver links. The channel gains are modeled as free space path loss where the transmitter-to-IRS and IRS-to-receiver distances are 2000λ (e.g., 120 m for carrier frequency 5 GHz). Fig. 7 shows $\|\mathbf{H}_{n,m}^{(j,i)}\|_F = |h_{n,m}^{(j)}|$ of receiver $j \in \{1, 2\}$ for one IRS tile versus the index of the adopted transmission mode. For comparison, we also plot $|h_{n,m}^{(j)}|$ sorted in a descending order. Fig. 6 confirms that for a given channel realization, not all transmission modes corresponding to the $17 \times 17 = 289$ reflection codebook elements are useful. In fact, for threshold $\delta = -75$ dB (almost 12 dB below the maximum $|h_{n,m}^{(j)}|$), only 13 modes out of the $17 \times 17 = 289$ possible modes are included in \mathcal{M} according to (25), which significantly reduces the complexity of the subsequent online optimization stage.

C. Online Optimization

The online configuration of the IRS requires the optimization of the binary mode selection variables, i.e., $s_{n,m}$, $\forall n, m$. Moreover, there are typically other system parameters, e.g., the precoder at the transmitter, that should be jointly optimized with $s_{n,m}$, $\forall n, m$. Therefore, in general, the IRS online optimization problem formulated based on the proposed channel model in (21) belongs to the class of *mixed integer programming* problems [23]. For this class of optimization problems, efficient solution methods have been developed in the literature [23]–[25]. Nevertheless, the specific solution approach required for optimizing an IRS-assisted system depends on the considered system model and the adopted QoS criterion, of course. Therefore, for concreteness, we focus on an IRS-assisted downlink system, in

which a BS with T transmit antennas sends data to N_r single-antenna users via linear precoding. For this special case, the received signal of the j -th user in (21) simplifies as follows

$$y^{(j)} = \sum_{n=0}^N \sum_{m \in \mathcal{M}} s_{n,m} \mathbf{h}_{n,m}^{(j)\text{H}} \mathbf{Q} \mathbf{u} + z^{(j)}, \quad j = 1, \dots, N_r, \quad (26)$$

where $\mathbf{u} \in \mathbb{C}^{N_r}$ contains the data for the N_r users and satisfies $\mathbb{E}\{\mathbf{u}\mathbf{u}^{\text{H}}\} = \mathbf{I}_{N_r}$ with $\mathbb{E}\{\cdot\}$ and \mathbf{I}_n denoting expectation and the $n \times n$ identity matrix, respectively. Moreover, $\mathbf{Q} = [\mathbf{q}_1, \dots, \mathbf{q}_{N_r}] \in \mathbb{C}^{T \times N_r}$ is a linear precoder matrix. Furthermore, $z^{(j)} \sim \mathcal{CN}(0, \sigma^2)$ denotes AWGN with mean zero and variance σ^2 impairing the j -th user and $\mathbf{h}_{n,m}^{(j)} = \mathbf{H}_{n,m}^{(j,1)\text{H}}$ represents the effective end-to-end channel between the BS and user j via the n -th tile of the IRS for the m -th transmission mode. With a slight abuse of notation, we introduce the additional index $n = 0$ and set $\mathbf{h}_{0,m}^{(j)} = \mathbf{H}_d^{(j,1)\text{H}}, \forall m$, to include the channel gains of the direct link.

Let $\mathbf{S} \in \{0, 1\}^{N \times M}$ be a matrix with $s_{n,m}$ as the element in its m -th row and n -th column. We wish to find the optimal \mathbf{S} and \mathbf{Q} that minimize the BS transmit power while guaranteeing a minimum signal-to-interference-noise ratio (SINR) for each user, i.e.,

$$\begin{aligned} & \underset{\mathbf{S} \in \{0,1\}^{N \times M}, \mathbf{Q} \in \mathbb{C}^{T \times N_r}}{\text{minimize}} && \text{tr}(\mathbf{Q}\mathbf{Q}^{\text{H}}) \\ & \text{subject to} && \text{C1: } \gamma_j(\mathbf{S}, \mathbf{Q}) \geq \gamma_j^{\text{thr}}, \quad \text{C2: } \sum_{m \in \mathcal{M}} s_{n,m} = 1, \quad \forall n, \end{aligned} \quad (27)$$

where $\text{tr}(\cdot)$ denotes the trace operator, γ_j^{thr} is the minimum required SINR of the j -th user, and $\gamma_j(\mathbf{S}, \mathbf{Q})$ denotes the SINR of the j -th user, which is given by

$$\gamma_j(\mathbf{S}, \mathbf{Q}) = \frac{\left| \sum_{n,m} s_{n,m} \mathbf{h}_{n,m}^{(j)\text{H}} \mathbf{q}_j \right|^2}{\sum_{j' \neq j} \left| \sum_{n,m} s_{n,m} \mathbf{h}_{n,m}^{(j)\text{H}} \mathbf{q}_{j'} \right|^2 + \sigma^2} = \frac{\sum_{n,m,n',m'} s_{n,m} s_{n',m'} \mathbf{h}_{n,m}^{(j)\text{H}} \mathbf{q}_j \mathbf{q}_{j'}^{\text{H}} \mathbf{h}_{n',m'}^{(j)}}{\sum_{j' \neq j, n, m, n', m'} s_{n,m} s_{n',m'} \mathbf{h}_{n,m}^{(j)\text{H}} \mathbf{q}_{j'} \mathbf{q}_{j'}^{\text{H}} \mathbf{h}_{n',m'}^{(j)} + \sigma^2}. \quad (28)$$

Problem (27) is non-convex due to 1) the product term $s_{n,m} \mathbf{q}_j$, 2) the quadratic form of the denominator and numerator of (28), and 3) the binary constraint $s_{n,m} \in \{0, 1\}$. Nevertheless, various approaches have been proposed in the literature to cope with such non-convex optimization problems [23]–[25]. In the following, we propose two efficient suboptimal solutions to (27).

1) Alternating Optimization-Based Solution: Hereby, we employ the following methods to cope with the aforementioned sources of non-convexity: *i)* To cope with the product term $s_{n,m} \mathbf{q}_j$, we use AO which finds a suboptimal solution of (27) by iteratively solving two subproblems. *ii)* To cope with the

quadratic term $s_{n,m}s_{n',m'}$ and the binary constraint $s_{n,m} \in \{0, 1\}$, we employ the big-M formulation. *iii)* To cope with the quadratic term $\mathbf{q}_j \mathbf{q}_j^H$, we employ SDP and rank relaxation. In addition, we show that the rank relaxation is tight.

Alternating Optimization: Straightforward AO of \mathbf{Q} and \mathbf{S} is not efficient as optimizing (27) with respect to \mathbf{S} for a given \mathbf{Q} returns the solution to which the problem was initialized. To address this issue, we decompose the precoder as $\mathbf{Q} = \sqrt{p} \tilde{\mathbf{Q}}$, where $p = \text{tr}(\mathbf{Q}\mathbf{Q}^H)$, i.e., $\text{tr}(\tilde{\mathbf{Q}}\tilde{\mathbf{Q}}^H) = 1$. Then, in Subproblem 1, we solve (27) jointly in p and \mathbf{S} for a given $\tilde{\mathbf{Q}}$, and in Subproblem 2, we solve (27) for \mathbf{Q} (or equivalently jointly for p and $\tilde{\mathbf{Q}}$) for a given \mathbf{S} . With this approach, transmit power p is reduced in both subproblems while guaranteeing the users' SINR requirements.

Subproblem 1 (Big-M Formulation and Mixed-Integer Linear Programming): Here, we solve (27) jointly in p and \mathbf{S} for a given $\tilde{\mathbf{Q}}$. The main challenge is the non-convex product term $\tilde{s}_{n,m}^{n',m'} p$. To address this issue, we use the Big-M formulation twice as follows [25]. Let us define auxiliary variable $\tilde{p}_{n,m}^{n',m'} = \tilde{s}_{n,m}^{n',m'} p$ where $\tilde{s}_{n,m}^{n',m'} = s_{n,m}s_{n',m'}$. Given that $s_{n,m}$ and $s_{n',m'}$ are binary, $\tilde{s}_{n,m}^{n',m'} = s_{n,m}s_{n',m'}$ and $\tilde{p}_{n,m}^{n',m'} = \tilde{s}_{n,m}^{n',m'} p$ can be equivalently written respectively as

$$\text{C3} : \tilde{s}_{n,m}^{n',m'} \in [0, 1], \tilde{s}_{n,m}^{n',m'} \leq s_{n,m}, \tilde{s}_{n,m}^{n',m'} \leq s_{n',m'}, \text{ and } \tilde{s}_{n,m}^{n',m'} \geq s_{n,m} + s_{n',m'} - 1 \quad (29)$$

$$\text{C4} : \tilde{p}_{n,m}^{n',m'} \in [0, p], \tilde{p}_{n,m}^{n',m'} \leq \tilde{s}_{n,m}^{n',m'} p^\circ, \text{ and } \tilde{p}_{n,m}^{n',m'} \geq p - (1 - \tilde{s}_{n,m}^{n',m'}) p^\circ, \quad (30)$$

where p° is an upper bound on p . Using the above new variables, constraint C1 is reformulated as

$$\tilde{\text{C1}} : \sum_{n,m,n',m'} \tilde{p}_{n,m}^{n',m'} \left[\mathbf{h}_{n,m}^{(j)H} \tilde{\mathbf{q}}_j \tilde{\mathbf{q}}_j^H \mathbf{h}_{n',m'}^{(j)} - \gamma_j^{\text{thr}} \sum_{j' \neq j} \mathbf{h}_{n,m}^{(j)H} \tilde{\mathbf{q}}_{j'} \tilde{\mathbf{q}}_{j'}^H \mathbf{h}_{n',m'}^{(j)} \right] \geq \gamma_j^{\text{thr}} \sigma^2. \quad (31)$$

Therefore, the first subproblem is given by

$$\text{P1: minimize } p \quad \text{subject to } \tilde{\text{C1}}, \text{C2, C3, C4.} \quad (32)$$

$$\begin{matrix} s_{n,m}, p \\ \tilde{s}_{n,m}^{n',m'}, \tilde{p}_{n,m}^{n',m'} \end{matrix}$$

Note that constraints $\tilde{\text{C1}}$, C3, and C4 are jointly linear in $s_{n,m}$, p , $\tilde{s}_{n,m}^{n',m'}$, and $\tilde{p}_{n,m}^{n',m'}$. Moreover, p , $\tilde{s}_{n,m}^{n',m'}$, and $\tilde{p}_{n,m}^{n',m'}$ are continuous variables whereas $s_{n,m}$ is binary. Therefore, P1 is a mixed binary-linear programming problem, for which many schemes have been developed to obtain efficient solutions, see e.g. [25] for a scheme based on binary relaxation with non-binary value penalization. Nevertheless, since these techniques are widely known and are efficiently integrated into popular solvers such as MOSEK as build-in blocks, we use these solvers directly to solve P1.

Subproblem 2 (SDP Formulation and Rank Relaxation): Defining the positive semi-definite

Algorithm 1 AO-based Online Optimization

- 1: **input:** Number of iterations N^{itr} , initial point $(\mathbf{S}^{(0)}, \mathbf{Q}^{(0)})$, channel coefficients $\mathbf{h}_{n,m}^{(j)}$, $\forall n, m, j$, and required SINRs γ_j^{thr} , $\forall j$.
 - 2: Set $p^{(0)} = \text{tr}(\mathbf{Q}^{(0)} \mathbf{Q}^{(0)\text{H}})$.
 - 3: **for** $i = 1, \dots, N^{\text{itr}}$ **do**
 - 4: Find (\mathbf{S}^*, p^*) as the solution of P1 in (32) for $(\mathbf{Q}^{(i-1)}, p^{(i-1)})$, and update $\mathbf{S}^{(i)} = \mathbf{S}^*$.
 - 5: Find \mathbf{Q}_j^* , $\forall j$, as the solution of P2 in (34) for $\mathbf{S}^{(i)}$ and update $\mathbf{Q}_j^{(i)} = \mathbf{Q}_j^*$.
 - 6: Set $\mathbf{Q}^{(i)} = [\mathbf{q}_1^{(i)}, \dots, \mathbf{q}_{N_r}^{(i)}]$ with $\mathbf{q}_j^{(i)} = \sum_k \lambda_k \boldsymbol{\nu}$, $\forall j$, where λ_k , $\forall k$, are the non-zero eigenvalues of $\mathbf{Q}_j^{(i)}$ and $\boldsymbol{\nu}$ is the eigenvector corresponding to the largest eigenvalue.
 - 7: Set $p^{(i)} = \text{tr}(\mathbf{Q}^{(i)} \mathbf{Q}^{(i)\text{H}})$.
 - 8: **end for**
 - 9: **output:** $\mathbf{Q} = \mathbf{Q}^{(N^{\text{itr}})}$ and $\mathbf{S} = \mathbf{S}^{(N^{\text{itr}})}$.
-

Algorithm 2 Greedy Iterative Online Optimization

- 1: **input:** Channel coefficients $\mathbf{h}_{n,m}^{(j)}$, $\forall n, m, j$, and required SINRs γ_j^{thr} , $\forall j$.
 - 2: Set $[\mathbf{S}]_{0,1} = 1$ and $[\mathbf{S}]_{n,m} = 0$, $\forall (n, m) \neq (0, 1)$.
 - 3: **for** $i = 1, \dots, N$ **do**
 - 4: Find \mathbf{Q}_j^* , $\forall j$, as the solution of P2 in (34) for \mathbf{S} and update $\mathbf{Q}_j^{(i)} = \mathbf{Q}_j^*$.
 - 5: Set $\mathbf{Q}^{(i)} = [\mathbf{q}_1^{(i)}, \dots, \mathbf{q}_{N_r}^{(i)}]$ with $\mathbf{q}_j^{(i)} = \sum_k \lambda_k \boldsymbol{\nu}$, $\forall j$, where λ_k , $\forall k$, are the non-zero eigenvalues of $\mathbf{Q}_j^{(i)}$ and $\boldsymbol{\nu}$ is the eigenvector corresponding to the largest eigenvalue.
 - 6: Select user j^* based on (35).
 - 7: Select the transmission mode of the i -th tile as m^* based on (36) and set $[\mathbf{S}]_{i,m^*} = 1$.
 - 8: **end for**
 - 9: Set $\mathbf{S}^* = \mathbf{S}$ and find \mathbf{Q}_j^* , $\forall j$, as the solution of P2 in (34) for \mathbf{S}^* .
 - 10: Set $\mathbf{Q}^* = [\mathbf{q}_1^*, \dots, \mathbf{q}_{N_r}^*]$ with $\mathbf{q}_j^* = \sum_k \lambda_k \boldsymbol{\nu}$, $\forall j$, where λ_k , $\forall k$, are the non-zero eigenvalues of \mathbf{Q}_j^* and $\boldsymbol{\nu}$ is the eigenvector corresponding to the largest eigenvalue.
 - 11: **output:** \mathbf{Q}^* and \mathbf{S}^* .
-

auxiliary matrix $\mathbf{Q}_j = \mathbf{q}_j \mathbf{q}_j^{\text{H}}$, constraint C1 is reformulated as follows

$$\widetilde{\text{C1}}: \quad \text{tr}(\bar{\mathbf{h}}_{n,m}^{(j)} \bar{\mathbf{h}}_{n',m'}^{(j)\text{H}} \mathbf{Q}_j) - \gamma_j^{\text{thr}} \sum_{j' \neq j} \text{tr}(\bar{\mathbf{h}}_{n,m}^{(j)} \bar{\mathbf{h}}_{n',m'}^{(j)\text{H}} \mathbf{Q}_{j'}) \geq \gamma_j^{\text{thr}} \sigma^2, \quad (33)$$

where $\bar{\mathbf{h}}_{n,m}^{(j)} = \sum_{n,m} s_{n,m} \mathbf{h}_{n,m}^{(j)}$. Note that, by definition, \mathbf{Q}_j has rank one which imposes a non-convex constraint, i.e., $\text{rank}(\mathbf{Q}_j) = 1$, $\forall j$, has to hold where $\text{rank}(\cdot)$ denotes the rank of a matrix. Nevertheless, the following lemma formally states that we can recover the optimal solution after dropping the rank constraint.

Lemma 1: There exists a \mathbf{Q}_j , $\forall j$, as the solution to problem

$$\text{P2: minimize}_{\mathbf{Q}_j \in \mathbb{C}^{T \times T}} \sum_{j=1}^{N_r} \text{tr}(\mathbf{Q}_j) \quad \text{subject to} \quad \widetilde{\text{C1}}, \text{C5: } \mathbf{Q}_j \succeq \mathbf{0}, \quad (34)$$

that has a rank equal to one, i.e., $\text{rank}(\mathbf{Q}_j) = 1$, $\forall j$.

Proof: The proof is provided in Appendix C. ■

The proposed AO-based online optimization is summarized in Algorithm 1. Note that the proof of Lemma 1 shows that \mathbf{Q}_j as a solution of (34) has either a rank equal to one or facilitates the construction of another feasible solution with identical objective function value that has rank one, see line 6 of Algorithm 1. Let us emphasize the following two challenges of Algorithm 1. 1) Recall that all AO-based algorithms are prone to getting trapped in local optima. Therefore, starting from a “good” initial point is crucial. 2) Subproblem P1 is a mix-integer programming problem and the big-M

formulation employed to construct this subproblem introduces a large number of variables which scales with $|\mathcal{M}|^2 N^2$. In the following, we propose a greedy algorithm for the optimization of \mathbf{S} to avoid the complexity of Subproblem P1. On the other hand, if the complexity of Subproblem P1 can be accommodated, the greedy algorithm can provide an initial point for Algorithm 1 to address the first challenge.

2) **Greedy Iterative Solution:** The proposed greedy algorithm is performed in N iterations where *one tile* is configured in each iteration. In particular, this algorithm involves the following stages:

Stage 1 (Precoder Design): In each iteration, we first solve P2 in (34) for a given \mathbf{S} obtained from the previous iteration. Note that in the first iteration, we use $[\mathbf{S}^{(0)}]_{0,1} = 1$ and $[\mathbf{S}^{(0)}]_{n,m} = 0, \forall (n, m) \neq (0, 1)$, i.e., only the direct link exists. Let $\mathbf{Q}^{(i)} = [\mathbf{q}_1^{(i)}, \dots, \mathbf{q}_{N_r}^{(i)}]$ denote the precoder designed in the i -th iteration.

Stage 2 (User Selection): In the i -th iteration, we configure the i -th tile such that it improves the channel of one user. Since our goal is to minimize the BS's transmit power, we choose the user which contributes most to the power consumption of the BS, i.e.,

$$j^* = \operatorname{argmax}_{j \in \{1, \dots, N_r\}} \|\mathbf{q}_j^{(i)}\|_2. \quad (35)$$

Stage 3 (IRS Configuration): Now, from the tile codebook \mathcal{M} , we select that element which improves the end-to-end channel gain of the selected user j^* the most, i.e.,

$$m^* = \operatorname{argmax}_{m \in \mathcal{M}} \left\| \mathbf{h}_{i,m}^{(j^*)} + \sum_{n=1}^{i-1} \sum_{m' \in \mathcal{M}} s_{n,m'} \mathbf{h}_{n,m'}^{(j^*)} \right\|_2. \quad (36)$$

Then, we set $[\mathbf{S}]_{i,m^*} = 1$.

After N iterations, we have readily determined \mathbf{S} . Thereby, we solve P2 in (34) for the obtained \mathbf{S} to optimize \mathbf{Q} . Algorithm 2 summarizes the proposed greedy algorithm.

D. Channel Estimation

A detailed treatment of the channel estimation problem is beyond the scope of this paper and is left for future work. Nevertheless, we briefly explain how the proposed offline codebook design and the end-to-end channel model formulation in (21) can be exploited to simplify the channel acquisition problem. In particular, considering the model in (21), the end-to-end channel has to be estimated only for the transmission modes contained in the offline codebook. In other words, for each transmission mode, the IRS sets the unit cells according to the transmission mode, the BS sends a pilot signal, and the

TABLE I
DEFAULT VALUES OF SYSTEM PARAMETERS.

Parameter	T	N_r	N	L_x, L_y	d_x, d_y	L_e	ρ_{eff}	$(\mathcal{B}_x , \mathcal{B}_y , \mathcal{B}_0)$	$ \mathcal{M} $	γ_j^{thr}	N_0	N_F	W	
Value	16 (4×4)	2	9 (3×3)	10λ	$\lambda/2$	$0.8d_x$	0.4	(17, 17, 4)	36	10 dB	-174 dBm/Hz	6 dB	20 MHz	
Parameter	(ρ_d, ρ_t, ρ_r)				(L_d, L_t, L_r)		$(\hat{h}_d, \hat{h}_t, \hat{h}_r)$		(b_d, b_t, b_r)		Range of ϕ and φ		Range of θ	
Value	$(4, 4, 0.4) \times 10^3 \lambda$ (e.g. (400, 400, 40) m at 3 GHz)				(1, 2, 2)		(-40, 0, 0) dB		(0, 0, 0)		[0, 2π]		BS, IRS: [0, $\pi/4$], users: [0, π]	

user estimates the end-to-end channel (or the related physical parameters). In practice, for the proposed model, it is not even required to estimate the channel for all transmission modes and the channel estimation procedure can be terminated as soon as few satisfactory transmission modes have been identified, according to e.g. (25). The search for useful transmission modes can be performed efficiently using hierarchical multi-resolution codebooks, see e.g. [31] for the application of such codebooks for channel estimation in millimeter wave communication systems.

IV. SIMULATION RESULTS

In this section, we evaluate the performance of the resource allocation schemes derived in Section III-C. We assume that both the direct and IRS-assisted links exist (i.e., no blockage); however, the direct link is severely shadowed, which motivates the deployment of the IRS. The channel gain for each effective path (i.e., the diagonal elements of $\Sigma_d^{(j)}$, Σ_t , and $\Sigma_r^{(j)}$) is modeled as $h_i = \sqrt{\bar{h}_i \hat{h}_i \tilde{h}_i}$, $i \in \{d, r, t\}$, where $\bar{h}_i = \left(\frac{\lambda}{4\pi\rho_i}\right)^2$, \hat{h}_i , and $\tilde{h}_i \sim \mathcal{CN}(0, 1)$ represent the free-space path-loss, large-scale shadowing/blockage, and small-scale Rayleigh fading, respectively, and the subscripts d , t , and r refer to the BS-to-user, BS-to-IRS, and IRS-to-user paths, respectively. The number of paths (scatterers) for the BS-to-user, BS-to-IRS, and IRS-to-user links are denoted by L_d , L_t , and L_r , respectively. The AoAs and AoDs at BS and IRS are generated as uniformly distributed random variables. We assume that the noise power at the receiver is given by $\sigma^2 = WN_0N_F$ where W is the bandwidth, N_0 represents the noise power spectral density, and N_F denotes the noise figure. The simulation results shown in this section have been averaged over 10^3 random channel realizations. We focus on IRSs with discrete tiles and the phase shift design in Proposition 2. The offline codebook is designed based on uniform discretization of $\bar{\beta}_x$, $\bar{\beta}_y$, and $\bar{\beta}_0$, as discussed in Section III-A. For online optimization, we select a fixed number of transmission modes from the reflection codebook, $\mathcal{B}_x \times \mathcal{B}_y$, for each user j based on the strength of the corresponding end-to-end channel gain $\|\mathbf{h}_{n,m}^{(j)}\|_2$. Moreover, we include the entire wavefront phase codebook \mathcal{B}_0 for online optimization to allow for an efficient superposition of the signals arriving at the users from different tiles and from the direct link. Unless otherwise stated, we adopt the default values of the system parameters provided in Table I.

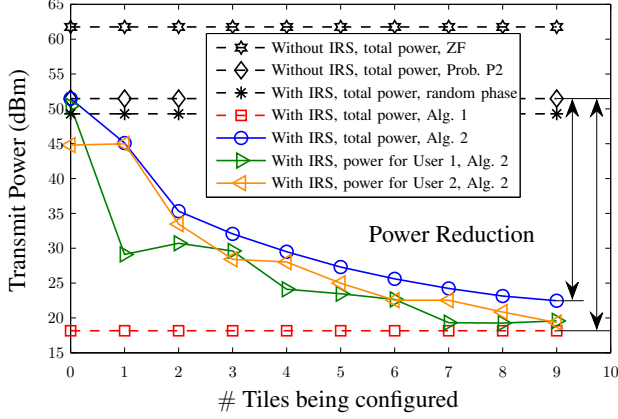


Fig. 8. Reduction of the transmit power for Algorithm 2 vs. the number of configured tiles (iterations) for one channel realization.

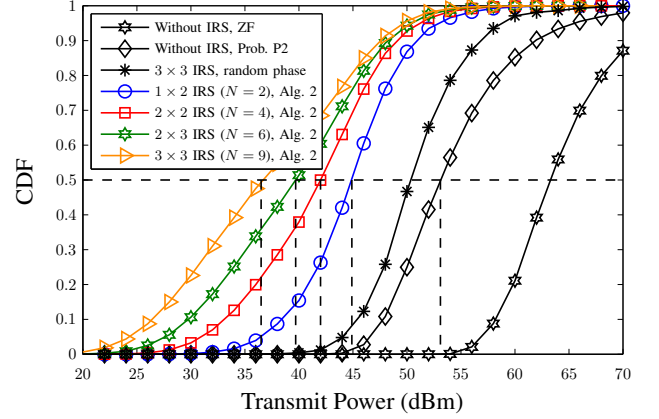


Fig. 9. CDF of the required transmit power for various IRS sizes and $\hat{h}_d = -50$ dB.

First, to illustrate how the proposed greedy Algorithm 2 behaves, we show in Fig. 8 the transmit power reduction as a function of the number of iterations for one channel realization. Fig. 8 confirms that a considerable power reduction is achieved in each iteration by configuring an additional tile. Moreover, we observe from Fig. 8 that, in each iteration, the power needed to serve the user that requires the higher BS transmit power to satisfy its QoS is significantly reduced which is in-line with the user selection strategy in line 6 of Algorithm 2. Overall, Fig. 8 shows that using Algorithm 2, an IRS with nine tiles of size $10\lambda \times 10\lambda$ can reduce the required transmit power by approximately 29 dBm compared to the case when the IRS is absent. For comparison, in Fig. 8, we also show the transmit power required for *i*) a zero-forcing precoder at the BS if no IRS is used [33], *ii*) the optimal precoder at the BS (according to problem P2) and random phase shifts at the IRS, and *iii*) the AO-based Algorithm 1 which employs the solution of the greedy scheme for initialization. We observe from Fig. 8 that to meet the users' QoS requirements without an IRS, the proposed optimal precoder requires a transmit power which is more than 10 dBm lower than that needed by the ZF precoder. Moreover, Fig. 8 shows that an IRS-assisted system with random phase shifts can reduce the transmit power by less than 2 dB compared to a system without IRS. Finally, for this channel realization, more than 3 dB power reduction is achieved by Algorithm 1 with respect to Algorithm 2. Nevertheless, extensive computer simulations have revealed that, for most channel realizations, the performance gain of the AO-based algorithm over the greedy algorithm is small, whereas the greedy algorithm is computationally much less complex. Therefore, in the remainder of this section, we adopt the proposed greedy algorithm.

In Fig. 9, we show the cumulative density function (CDF) of the required BS transmit power. This figure shows that the probability that the IRS can satisfy the users' QoS with a small transmit power

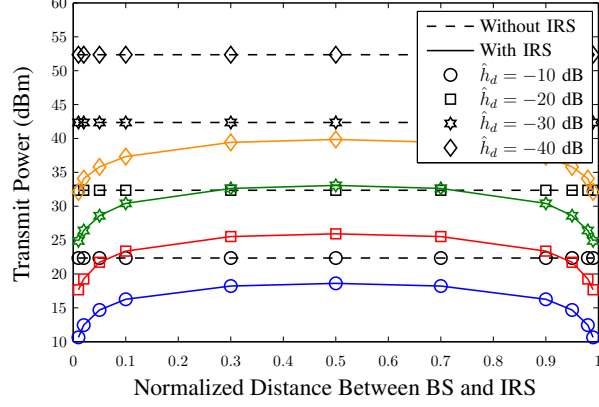


Fig. 10. Required transmit power vs. the distance between the BS and the IRS normalized to the distance between the BS and the users.

increases as the size of the IRS increases. For example, if the IRS is equipped with $N = 0, 2, 4, 6, 9$ tiles (i.e., $Q = 0, 800, 1600, 2400, 3600$ elements), for 50% of the channel realizations, the BS needs a transmit power of less than 53, 45, 42, 40, and 36 dBm, respectively, to satisfy the users' QoS. Nevertheless, Fig. 9 also suggests that there still exist channel realizations which require a high transmit power to meet the users' QoS requirements due to faded IRS-assisted links. This issue could be remedied by deploying more than one IRS and associating the users with the IRS that yields the strongest end-to-end channel. Similar to Fig. 8, we observe from Fig. 9 that an IRS with random phase shifts can only marginally reduce the required transmit power.

Next, we investigate the impact of the shadowing loss of the direct link, \hat{h}_d , and the position of the IRS on performance, where we assume $\rho_t + \rho_r = \rho_d = 4 \times 10^3 \lambda$ (e.g., 400, 240, 120, 42 m at carrier frequencies of 3, 5, 10, 28 GHz, respectively). In Fig. 10, we show the required transmit power vs. the distance between the BS and the IRS normalized to the distance between the BS and the users, i.e., ρ_t/ρ_d , for several values of \hat{h}_d . We observe from this figure that the required transmit power is minimized when the IRS is either close to the BS or close to the users, see [34] for a similar observation. Moreover, Fig. 10 shows that the relative amount of power saved by the IRS-assisted system compared to the system without IRS decreases as the direct link becomes stronger.

In Fig. 11, we show the required transmit power vs. the size of the offline reflection codebooks, $|\mathcal{B}_x| = |\mathcal{B}_y|$, for different values of $|\mathcal{M}|$ (number of transmission modes used for online optimization) and different sizes of wavefront phase codebook $|\mathcal{B}_0|$. We observe from Fig. 11 that for fixed $|\mathcal{M}|$, as the size of the reflection codebook increases, the required transmit power first decreases and then increases. The reason for this behavior is that when $|\mathcal{M}|$ is fixed but $|\mathcal{B}_x|$ and $|\mathcal{B}_y|$ are large, only the transmission modes that reflect the incident beam along angles around the AoD with the strongest path to the users

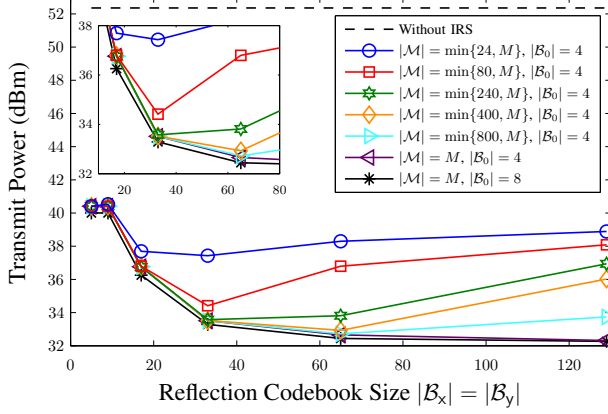


Fig. 11. Required transmit power vs. the size of offline reflection codebooks $|\mathcal{B}_x| = |\mathcal{B}_y|$ for different sizes of the selected online codebook $|\mathcal{M}|$, different sizes of wavefront phase codebook $|\mathcal{B}_0|$, and an IRS with $N = 9$ tiles each of size $10\lambda \times 10\lambda$.

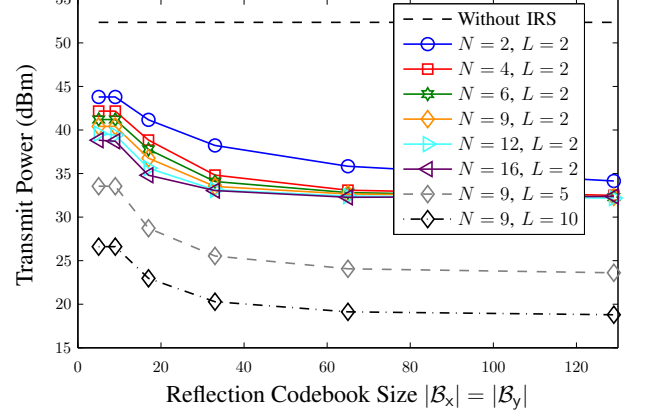


Fig. 12. Required transmit power vs. the size of offline reflection codebooks $|\mathcal{B}_x| = |\mathcal{B}_y|$ for $|\mathcal{B}_0| = 4$, $|\mathcal{M}| = M = |\mathcal{B}_x| \times |\mathcal{B}_y| \times |\mathcal{B}_0|$, different numbers of IRS tiles N while the total IRS area is $30\lambda \times 30\lambda$, and different numbers of scatterers $L_t = L_r = L$.

are selected and the transmission modes reflecting along other AoDs are removed by the pre-selection of \mathcal{M} and do not participate in the online optimization. This has a negative impact on the system performance for large $|\mathcal{B}_x|$ and $|\mathcal{B}_y|$. However, if the pre-selection is removed, i.e., $|\mathcal{M}| = M$, then the required transmit power monotonically decreases as $|\mathcal{B}_x|, |\mathcal{B}_y|$ increase. On the other hand, recall that the pre-selection of \mathcal{M} reduces the complexity of online optimization, cf. (34) and (36). In fact, for $|\mathcal{B}_x| = |\mathcal{B}_y| = 17$ and $|\mathcal{B}_0| = 4$, using $|\mathcal{M}| = 24$ transmission modes (out of the $M = 4 \times 17 \times 17 = 1156$ entries of the offline codebook) yields an approximately only one dBm higher transmit power compared to the case when all $M = 1156$ elements of the offline codebook are used for online optimization. Moreover, Fig. 11 suggests that an additional power reduction can be achieved by increasing the size of the wavefront phase codebook from 4 to 8; nevertheless, this gain is small.

Finally, we study the impact of the tile size on the system performance. Fig. 12 shows the required transmit power vs. the size of offline reflection codebooks $|\mathcal{B}_x| = |\mathcal{B}_y|$ for different numbers of tiles N while the total IRS size is kept fixed as $30\lambda \times 30\lambda$ and different numbers of channel scatterers for the BS-to-IRS link, L_t , and IRS-to-user links, L_r , where we assumed $L_t = L_r = L$. As can be seen from Fig. 12, the required transmit power decreases as the number of tiles increases; however, increasing the number of tiles beyond $N = 9$ yields only a small power reduction particularly for large reflection codebook sizes. In other words, this figure confirms that online optimization of the large number of sub-wavelength unit cells on the IRS (e.g., 3600 unit cells for the example in Fig. 12) is not necessary and a much smaller number of tiles (e.g., $N = 9$ in Fig. 12) is sufficient for efficient online optimization. Nevertheless, we emphasize that the required numbers of tiles depends on various system parameters

including the number of transmitters/receivers and the number of scatterers in the channel. Furthermore, we observe from Fig. 12 that as the number of channel scatterers in the environment increases, the required transmit power significantly decreases. This is due to the fact that as the number of scatterers increases, there are more AoAs and AoDs for the IRS to exploit for selecting strong BS-to-IRS and IRS-to-user paths.

V. CONCLUSIONS AND OUTLOOK

In this paper, we presented a scalable optimization framework for large IRSs based on a physics-based channel model for IRS-assisted wireless systems. In particular, we partitioned the IRS unit cells into several subsets, i.e., tiles, and derived the tile response function for both continuous and discrete tiles. Moreover, we developed a physics-based end-to-end channel model for IRS-assisted communications and proposed to optimize the IRS in two stages: an offline design stage and an online optimization stage. For offline design, we jointly designed the unit cells of a tile for the support of different transmission modes. For online optimization, we formulated a mixed-integer programming problem, where for each fading realization, the objective is to select the best transmission mode for each tile such that a desired QoS is maximized. Moreover, for an exemplary downlink system, we studied the minimization of the BS transmit power subject to QoS constraints for the users and derived two corresponding algorithms employing AO and a greedy approach, respectively. Computer simulations results showed that the proposed modeling and optimization framework can be used to efficiently configure large IRSs containing thousands of elements. Furthermore, we showed that increasing the number of tiles for a given IRS size beyond a certain number yields a negligible performance improvement.

Most existing methods developed in the literature for online configuration of IRS-assisted wireless systems directly optimize the phases of the Q unit cells of the IRS. Therefore, the complexity of these algorithms scales with the number of unit cells, Q , and the number of possible phases per unit cell, $|\mathcal{B}|$. On the other hand, the proposed model enables the design of algorithms for online optimization of IRS-assisted wireless systems whose complexity scales with the number of tiles, N , and the number of transmission modes, M , which yields a complexity that is in general much smaller than that for the conventional approach. This motivates the application of the proposed IRS-assisted channel model for the design of scalable algorithms for different wireless network architectures and different design goals in future research. Another interesting topic for future work is the development of channel estimation techniques based on the proposed end-to-end channel model for IRS-assisted systems.

APPENDIX A
PROOF OF PROPOSITION 1

The electric field \mathbf{E}_r is a vector that is defined for each point in space by (6) and (7). Using a spherical coordinate system, at any point (ρ, θ, ϕ) , the electric field \mathbf{E}_r (and the magnetic field \mathbf{H}_r) is a vector that in general has components in the radial \mathbf{e}_ρ , elevation \mathbf{e}_θ , and azimuth \mathbf{e}_ϕ directions. However, the elevation and azimuth components decay with $1/\rho$ whereas the radial component decays faster. Therefore, in the far field, the impact of the radial component becomes negligible and the electric and magnetic fields become perpendicular to the propagation direction [21, Ch. 6.7]. In addition, for the elevation and azimuth components, \mathbf{E}_r and \mathbf{H}_r in (6) simplify to

$$\mathbf{E}_r = -j\omega\mathbf{V} \quad \text{and} \quad \mathbf{H}_r = -j\frac{\omega}{\eta}\mathbf{e}_\rho \times \mathbf{V}. \quad (37)$$

To find the elevation and azimuth components of the electric and magnetic fields at the observation point specified by $(\rho_r, \theta_r, \phi_r)$, we first find the corresponding generating components of \mathbf{J}_r using (5) as

$$J_\theta = \tilde{J}_\theta e^{jk[A_x(\Psi_t)x + A_y(\Psi_t)y]} e^{j\beta(x,y)} \quad \text{and} \quad J_\phi = \tilde{J}_\phi e^{jk[A_x(\Psi_t)x + A_y(\Psi_t)y]} e^{j\beta(x,y)}, \quad (38)$$

where $\tilde{J}_\theta = J_x \cos(\theta_r) \cos(\phi_r) + J_y \cos(\theta_r) \sin(\phi_r)$ and $\tilde{J}_\phi = -J_x \sin(\phi_r) + J_y \cos(\phi_r)$. Therefore, the elevation and azimuth components of $\mathbf{V}(\Psi_r)$ in (7), denoted by $V_\theta(\theta_r)$ and $V_\phi(\phi_r)$, respectively, are found as

$$V_\theta(\theta_r) = \frac{\mu e^{-jk\rho_r}}{4\pi\rho_r} \int_{x=-L_x/2}^{L_x/2} \int_{y=-L_y/2}^{L_y/2} \tilde{J}_\theta e^{jk[A_x(\Psi_t)x + A_y(\Psi_t)y]} e^{j\beta(x,y)} e^{jk\sqrt{x^2+y^2}\cos(\alpha)} dx dy \quad (39a)$$

$$V_\phi(\phi_r) = \frac{\mu e^{-jk\rho_r}}{4\pi\rho_r} \int_{x=-L_x/2}^{L_x/2} \int_{y=-L_y/2}^{L_y/2} \tilde{J}_\phi e^{jk[A_x(\Psi_t)x + A_y(\Psi_t)y]} e^{j\beta(x,y)} e^{jk\sqrt{x^2+y^2}\cos(\alpha)} dx dy. \quad (39b)$$

In the far field, we obtain $\cos(\alpha) = \frac{(A_x(\Psi_r), A_y(\Psi_r), A_z(\Psi_r)) \cdot (x, y, 0)}{\|(x, y, 0)\|} = \frac{A_x(\Psi_r)x + A_y(\Psi_r)y}{\sqrt{x^2+y^2}}$. Using (37), (39a), and the phase shift $\beta(x, y)$ in (8), the elevation component of the electric vector field, denoted by $E_r^\theta(\theta_r)$, is obtained as

$$E_r^\theta(\theta_r) = \tilde{E}_\theta \int_{x=-L_x/2}^{L_x/2} e^{jk[A_x(\Psi_t, \Psi_r) - A_x(\Psi_t^*, \Psi_r^*)]x} dx \int_{y=-L_y/2}^{L_y/2} e^{jk[A_y(\Psi_t, \Psi_r) - A_y(\Psi_t^*, \Psi_r^*)]y} dy, \quad (40)$$

where $\tilde{E}_\theta = \frac{-jk\eta e^{-jk\rho_r + j\beta_0}}{4\pi\rho_r} \tilde{J}_\theta$. To solve the integrals in (40), we use the integral identity $\int_{z=-c/2}^{c/2} e^{jAz} dz = c \operatorname{sinc}\left(\frac{Ac}{2}\right)$ [21, p. 593]. This leads to

$$E_r^\theta(\theta_r) = \tilde{E}_\theta L_x L_y \operatorname{sinc}\left(\frac{kL_x[A_x(\Psi_t, \Psi_r) - A_x(\Psi_t^*, \Psi_r^*)]}{2}\right) \operatorname{sinc}\left(\frac{kL_y[A_y(\Psi_t, \Psi_r) - A_y(\Psi_t^*, \Psi_r^*)]}{2}\right). \quad (41)$$

The azimuth component of the electric vector field, denoted by $E_r^\phi(\phi_r)$, is obtained in a similar manner as follows

$$E_r^\phi(\phi_r) = \tilde{E}_\phi L_x L_y \operatorname{sinc}\left(\frac{kL_x[A_x(\Psi_r) - A_x(\Psi_r^*)]}{2}\right) \operatorname{sinc}\left(\frac{kL_y[A_y(\Psi_r) - A_y(\Psi_r^*)]}{2}\right), \quad (42)$$

where $\tilde{E}_\phi = \frac{-jk\eta e^{-jk\rho_r + j\beta_0}}{4\pi\rho_r} \tilde{J}_\phi$. Recalling that the radial component is negligible, the magnitude of the electric field (up to a sign since the sinc functions can be negative) is found as

$$\begin{aligned} \|\mathbf{E}_r(\Psi_r)\| &= \sqrt{|E_r^\theta(\theta_r)|^2 + |E_r^\phi(\phi_r)|^2} \\ &= CL_x L_y \operatorname{sinc}\left(\frac{kL_x[A_x(\Psi_t, \Psi_r) - A_x(\Psi_t^*, \Psi_r^*)]}{2}\right) \operatorname{sinc}\left(\frac{kL_y[A_y(\Psi_t, \Psi_r) - A_y(\Psi_t^*, \Psi_r^*)]}{2}\right), \end{aligned} \quad (43)$$

where $C = \sqrt{|\tilde{E}_\theta|^2 + |\tilde{E}_\phi|^2} = \frac{k\eta}{4\pi\rho_r} \sqrt{\tilde{J}_\theta^2 + \tilde{J}_\phi^2} = \frac{E_0}{\sqrt{4\pi\rho_r^2}} \frac{\sqrt{4\pi\rho_{\text{eff}}}}{\lambda} \tilde{g}(\Psi_t, \Psi_r)$ and $\tilde{g}(\Psi_t, \Psi_r)$ is given in (10). Substituting $\|\mathbf{E}_r(\Psi_r)\|$ into (1) leads to the magnitude of $g(\Psi_t, \Psi_r)$ given in (9). Moreover, the phase of $g(\Psi_t, \Psi_r)$ (up to a sign) is given by $\pi/2 + \beta_0$. This completes the proof.

APPENDIX B

PROOF OF PROPOSITION 2

The proof is similar to that provided in [35, p. 963] for the analysis of uniform planar arrays. In particular, employing identities

$$\sum_{n=0}^{N-1} a^n = \frac{1 - a^N}{1 - a} \quad \text{and} \quad \sin(b) = \frac{e^{jb} - e^{-jb}}{2j}, \quad (44)$$

and setting $a = e^{jA}$, we have

$$\sum_{n=0}^{N-1} e^{jAn} = \frac{1 - e^{jNA}}{1 - e^{jA}} = \frac{e^{jNA/2}}{e^{jA/2}} \times \frac{e^{-jNA/2} - e^{jNA/2}}{e^{-jA/2} - e^{jA/2}} = e^{j(N-1)A/2} \times \frac{\sin(NA/2)}{\sin(A/2)}. \quad (45)$$

Now, using the above identity and the β_{n_x, n_y} given in (14), we have

$$\sum_{n_x = -\frac{Q_x}{2} + 1}^{\frac{Q_x}{2}} e^{jk d_x [A_x(\Psi_t) + A_x(\Psi_r)] n_x + j\beta_{n_x}} \stackrel{(a)}{=} \sum_{\tilde{n}_x = 0}^{Q_x - 1} e^{jk d_x [A_x(\Psi_t, \Psi_r) - A_x(\Psi_t^*, \Psi_r^*)] (\tilde{n}_x - Q_x/2 + 1) + j\beta_0/2}$$

$$= e^{j\beta_0/2} e^{-jW_x(\frac{Q_x}{2}-1)} \sum_{n_x=0}^{Q_x-1} e^{jW_x n_x} = e^{j\beta_0/2} e^{jW_x/2} \times \frac{\sin(Q_x W_x/2)}{\sin(W_x/2)}, \quad (46)$$

where $W_x = kd_x[A_x(\Psi_t, \Psi_r) - A_x(\Psi_t^*, \Psi_r^*)]$ and for equality (a), we used $\tilde{n}_x = n_x + \frac{Q_x}{2} - 1$. Applying the same approach to simplify to the second sum in (13), we obtain the amplitude of $g^d(\Psi_t, \Psi_r)$ (up to a sign) as

$$g_{||}^d(\Psi_t, \Psi_r) = |S_e(\Psi_t, \Psi_r)| \times \frac{\sin(Q_x W_x/2)}{\sin(W_x/2)} \times \frac{\sin(Q_y W_y/2)}{\sin(W_y/2)}, \quad (47)$$

where $W_y = kd_y[A_y(\Psi_t, \Psi_r) - A_y(\Psi_t^*, \Psi_r^*)]$. The phase of $g^d(\Psi_t, \Psi_r)$ (up to a sign) can be found as

$$g_{\angle}^d(\Psi_t, \Psi_r) = \angle S_e(\Psi_t, \Psi_r) + \frac{W_x}{2} + \frac{W_y}{2} + \beta_0 = \frac{\pi}{2} + \frac{W_x}{2} + \frac{W_y}{2} + \beta_0. \quad (48)$$

This leads to the amplitude and phase functions given in Proposition 2 and concludes the proof.

APPENDIX C

PROOF OF LEMMA 1

The problem in (34) is jointly convex with respect to the optimization variables \mathbf{Q}_j and satisfies Slater's constraint qualification [36]. Hence, strong duality holds and solving the dual problem of (34) yields the optimal primal solution. The Lagrangian dual function of the problem in (34) can be formulated as

$$\mathcal{L}(\mathbf{Q}_j, \lambda_j, \mathbf{X}_j, \forall j) = \sum_j \text{tr}(\mathbf{Q}_j) - \sum_j \text{tr}(\mathbf{X}_j \mathbf{Q}_j) - \sum_j \lambda_j \Upsilon_j(\mathbf{Q}_j, \forall j), \quad (49)$$

where $\Upsilon_j(\mathbf{Q}_j, \forall j) = \sum_{n,m,n',m',j} \tilde{s}_{n,m}^{n',m'} [\text{tr}(\mathbf{h}_{n,m}^{(j)} \mathbf{h}_{n',m'}^{(j)H} \mathbf{Q}_j) - \gamma_j^{\text{thr}} \sum_{\substack{j' \neq j \\ \sim}} \text{tr}(\mathbf{h}_{n,m}^{(j')} \mathbf{h}_{n',m'}^{(j')H} \mathbf{Q}_{j'})] - \gamma_j^{\text{thr}} \sigma^2$, and λ_j and \mathbf{X}_j

denote the associated Lagrange multipliers for constraints C1 and C5, respectively. Next, we highlight the following Karush Kuhn Tucker (KKT) necessary optimality conditions that the optimal solution \mathbf{Q}_j^* , λ_j^* , and \mathbf{X}_j^* has to meet:

$$\begin{aligned} \text{K1: } \mathbf{Q}_j^* \succeq \mathbf{0}, \mathbf{X}_j^* \succeq \mathbf{0}, \lambda_j^* \geq 0, \quad \text{K2: } \mathbf{X}_j^* \mathbf{Q}_j^* = \mathbf{0}, \lambda_j^* \Upsilon_j(\mathbf{Q}_j^*, \forall j) = 0 \\ \text{K3: } \nabla_{\mathbf{Q}_j} \mathcal{L}(\mathbf{Q}_j, \lambda_j, \mathbf{X}_j, \forall j) = \mathbf{0} \quad \Rightarrow \quad \mathbf{X}_j^* = \mathbf{I} - \Delta_j, \end{aligned} \quad (50)$$

where $\Delta_j = \sum_{n,m,n',m'} \tilde{s}_{n,m}^{n',m'} (\lambda_j^* - \sum_{j' \neq j} \lambda_{j'}^* \gamma_{j'}^{\text{thr}}) \mathbf{h}_{n,m}^{(j)} \mathbf{h}_{n',m'}^{(j)H}$. First, note that for K2 to hold, the columns of \mathbf{Q}_j^* should belong to the null space of \mathbf{X}_j^* , which implies that $\text{rank}(\mathbf{Q}_j^*) \leq T - \text{rank}(\mathbf{X}_j^*)$. Let us rewrite $\Delta_j = \sum_i \delta_i \mathbf{u}_i \mathbf{u}_i^H$, where δ_i and \mathbf{u}_i are the eigenvalues and the corresponding eigenvectors of Δ_j , respectively. Moreover, we assume that the δ_i are arranged in a descending order and define

$\delta^{\max} = \max_i \delta_i = \delta_1$. Notice that $\delta^{\max} > 1$ cannot hold since we can conclude from K3 that at least one eigenvalue of \mathbf{X}_j^* is negative which contradicts condition $\mathbf{X}_j^* \succeq \mathbf{0}$ in K1. On the other hand, if $\delta^{\max} < 1$ holds, we can conclude from K3 that \mathbf{X}_j^* has full rank, i.e., $\text{rank}(\mathbf{X}_j^*) = T$, which implies that for K2 to hold, we must have $\text{rank}(\mathbf{Q}_j^*) \leq T - T = 0$, i.e., $\mathbf{Q}_j^* = \mathbf{0}$, which violates $\widetilde{\text{C1}}$ in (34) for $\gamma_j^{\text{thr}} > 0$. Finally, for $\delta^{\max} = 1$, we study the general case where there are r eigenvalues equal to one, i.e., $\delta_1 = \dots = \delta_r = 1$. For K2 to hold, we can write $\mathbf{Q}_j^* = \sum_{i=1}^r c_i \mathbf{u}_i \mathbf{u}_i^H$, where c_i are some coefficients. In general, $\text{rank}(\mathbf{Q}_j^*) \leq r$; however, we show in the following that for any \mathbf{Q}_j^* with rank $r > 1$, we can construct another solution $\widetilde{\mathbf{Q}}_j^* = (\sum_{i=1}^r c_i) \mathbf{u}_1 \mathbf{u}_1^H$ which has rank one and does not affect the Lagrangian function, i.e.,

$$\mathcal{L}(\mathbf{Q}_j, \lambda_j, \mathbf{X}_j, \forall j) = \sum_j \text{tr}(\mathbf{Q}_j) - \sum_j \text{tr}(\mathbf{X}_j \mathbf{Q}_j) - \sum_j \lambda_j \Delta_j(\mathbf{Q}_j, \forall j) + \sum_j \lambda_j \gamma_j^{\text{thr}} \sigma^2. \quad (51)$$

We can readily confirm that $\text{tr}(\mathbf{Q}_j^*) = \text{tr}(\widetilde{\mathbf{Q}}_j^*) = \sum_{i=1}^r c_i$, $\mathbf{X}_j \mathbf{Q}_j^* = \mathbf{X}_j \widetilde{\mathbf{Q}}_j^* = \mathbf{0}$, and $\text{tr}(\Delta_j \mathbf{Q}_j^*) = \text{tr}(\Delta_j \widetilde{\mathbf{Q}}_j^*) = \sum_{i=1}^r c_i$. In summary, there always exists an optimal solution for (34) for which $\text{rank}(\mathbf{Q}_j^*) = 1$ holds. This completes the proof.

REFERENCES

- [1] M. Najafi, V. Jamali, R. Schober, and V. H. Poor, "Physics-based modeling of large intelligent reflecting surfaces for scalable optimization," *Submitted to Asilomar Conf. Sig., Sys., and Computers*, pp. 1–5, 2020.
- [2] M. D. Renzo, et. al, "Smart radio environments empowered by AI reconfigurable meta-surfaces: An idea whose time has come," *EURASIP J. Wireless Commun. Netw.*, vol. 129, May 2019.
- [3] C. Liaskos, S. Nie, A. Tsioliaridou, A. Pitsillides, S. Ioannidis, and I. Akyildiz, "A novel communication paradigm for high capacity and security via programmable indoor wireless environments in next generation wireless systems," *Ad Hoc Netw.*, vol. 87, pp. 1–16, 2019.
- [4] N. Kaina, M. Dupré, G. Lerosey, and M. Fink, "Shaping complex microwave fields in reverberating media with binary tunable metasurfaces," *Scientific Reports*, vol. 4, no. 1, pp. 1–8, 2014.
- [5] B. O. Zhu, J. Zhao, and Y. Feng, "Active impedance metasurface with full 360 reflection phase tuning," *Scientific Reports*, vol. 3, p. 3059, 2013.
- [6] Q. Wu and R. Zhang, "Intelligent reflecting surface enhanced wireless network via joint active and passive beamforming," *IEEE Trans. Wireless Commun.*, 2019.
- [7] V. Jamali, A. M. Tulino, G. Fischer, R. Müller, and R. Schober, "Scalable and energy-efficient millimeter massive MIMO architectures: Reflect-array and transmit-array antennas," in *Proc. IEEE Int. Conf. Commun. (ICC)*, May 2019, pp. 1–7.
- [8] W. Tang, M. Z. Chen, X. Chen, J. Y. Dai, Y. Han, M. Di Renzo, Y. Zeng, S. Jin, Q. Cheng, and T. J. Cui, "Wireless communications with reconfigurable intelligent surface: Path loss modeling and experimental measurement," *arXiv preprint arXiv:1911.05326*, 2019.
- [9] H. Yang, X. Cao, F. Yang, J. Gao, S. Xu, M. Li, X. Chen, Y. Zhao, Y. Zheng, and S. Li, "A programmable metasurface with dynamic polarization, scattering and focusing control," *Scientific Reports*, vol. 6, p. 35692, 2016.

- [10] L. Dai, B. Wang, M. Wang, X. Yang, J. Tan, S. Bi, S. Xu, F. Yang, Z. Chen, M. D. Renzo, C. Chae, and L. Hanzo, "Reconfigurable intelligent surface-based wireless communications: Antenna design, prototyping, and experimental results," *IEEE Access*, vol. 8, pp. 45 913–45 923, Mar. 2020.
- [11] X. Yu, D. Xu, Y. Sun, D. W. K. Ng, and R. Schober, "Robust and secure wireless communications via intelligent reflecting surfaces," *arXiv preprint arXiv:1912.01497*, 2019.
- [12] V. Jamali, A. Tulino, G. Fischer, R. Müller, and R. Schober, "Intelligent reflecting and transmitting surface aided millimeter wave massive MIMO," *arXiv preprint arXiv:1902.07670*, 2019.
- [13] C. Pan, H. Ren, K. Wang, W. Xu, M. ElKashlan, A. Nallanathan, and L. Hanzo, "Multicell MIMO communications relying on intelligent reflecting surface," *arXiv preprint arXiv:1907.10864*, 2019.
- [14] H. Guo, Y.-C. Liang, J. Chen, and E. G. Larsson, "Weighted sum-rate optimization for intelligent reflecting surface enhanced wireless networks," *arXiv preprint arXiv:1905.07920*, 2019.
- [15] P. Wang, J. Fang, X. Yuan, Z. Chen, H. Duan, and H. Li, "Intelligent reflecting surface-assisted millimeter wave communications: Joint active and passive precoding design," *arXiv preprint arXiv:1908.10734*, 2019.
- [16] Ö. Özdoğan, E. Björnson, and E. G. Larsson, "Intelligent reflecting surfaces: Physics, propagation, and pathloss modeling," *IEEE Commun. Lett.*, 2019.
- [17] E. Björnson and L. Sanguinetti, "Power scaling laws and near-field behaviors of massive MIMO and intelligent reflecting surfaces," *arXiv preprint arXiv:2002.04960*, 2020.
- [18] M. Di Renzo, F. H. Danufane, X. Xi, J. de Rosny, and S. Tretyakov, "Analytical modeling of the path-loss for reconfigurable intelligent surfaces—Anomalous mirror or scatterer?" *arXiv preprint arXiv:2001.10862*, 2020.
- [19] T. Bai, C. Pan, Y. Deng, M. ElKashlan, and A. Nallanathan, "Latency minimization for intelligent reflecting surface aided mobile edge computing," *arXiv preprint arXiv:1910.07990*, 2019.
- [20] Y. Cao, T. Lv, Z. Lin, W. Ni, and N. C. Beaulieu, "Delay-constrained joint power control, user detection and passive beamforming in intelligent reflecting surface assisted uplink mmWave system," *arXiv preprint arXiv:1912.10030*, 2019.
- [21] C. A. Balanis, *Advanced Engineering Electromagnetics*. John Wiley & Sons, 2012.
- [22] M. Najafi and R. Schober, "Intelligent reflecting surfaces for free space optical communications," in *Proc. IEEE Global Commun. Conf. (Globecom)*, Dec. 2019, pp. 1–7.
- [23] J. Lee and S. Leyffer, *Mixed Integer Nonlinear Programming*. Springer Science & Business Media, 2011, vol. 154.
- [24] D. W. K. Ng, E. S. Lo, and R. Schober, "Robust beamforming for secure communication in systems with wireless information and power transfer," *IEEE Trans. Wireless Commun.*, vol. 13, no. 8, pp. 4599–4615, Aug. 2014.
- [25] W. R. Ghanem, V. Jamali, Y. Sun, and R. Schober, "Resource allocation for multi-user downlink URLLC-OFDMA systems," in *Proc. IEEE Int. Conf. Commun. (ICC)*, May 2019, pp. 1–6.
- [26] F. Liu, O. Tsilipakos, A. Ptilakis, A. C. Tasolamprou, M. S. Mirmoosa, N. V. Kantartzis, D.-H. Kwon, M. Kafesaki, C. M. Soukoulis, and S. A. Tretyakov, "Intelligent metasurfaces with continuously tunable local surface impedance for multiple reconfigurable functions," *Physical Review Applied*, vol. 11, no. 4, p. 044024, 2019.
- [27] S. Abeywickrama, R. Zhang, and C. Yuen, "Intelligent reflecting surface: Practical phase shift model and beamforming optimization," *arXiv preprint arXiv:1907.06002*, 2019.
- [28] N. M. Estakhri and A. Alù, "Wave-front transformation with gradient metasurfaces," *Physical Review X*, vol. 6, no. 4, p. 041008, 2016.
- [29] V. S. Asadchy, M. Albooyeh, S. N. Tsvetkova, A. Díaz-Rubio, Y. Ra'idi, and S. Tretyakov, "Perfect control of reflection and refraction using spatially dispersive metasurfaces," *Physical Review B*, vol. 94, no. 7, p. 075142, 2016.
- [30] J. Y. Lau, "Reconfigurable transmitarray antennas," Ph.D. dissertation, University of Toronto, 2012.

- [31] A. Alkhateeb, O. El Ayach, G. Leus, and R. W. Heath, "Channel estimation and hybrid precoding for millimeter wave cellular systems," *IEEE J. Select. Topics Sig. Process.*, vol. 8, no. 5, pp. 831–846, Oct. 2014.
- [32] R. Ghanaatian, V. Jamali, A. Burg, and R. Schober, "Feedback-aware precoding for millimeter wave massive MIMO systems," Sep. 2019, pp. 1–7.
- [33] S. Hu and F. Rusek, "A generalized zero-forcing precoder with successive dirty-paper coding in miso broadcast channels," *IEEE Trans. Wireless Commun.*, vol. 16, no. 6, pp. 3632–3645, Jun. 2017.
- [34] E. Björnson, Ö. Özdogan, and E. G. Larsson, "Intelligent reflecting surface vs. decode-and-forward: How large surfaces are needed to beat relaying?" *IEEE Wireless Commun. Lett.*, vol. 2, no. 9, pp. 244–248, Feb. 2020.
- [35] C. A. Balanis, *Antenna Theory: Analysis and Design*. John Wiley & Sons, 2005.
- [36] S. Boyd and L. Vandenberghe, *Convex Optimization*. Cambridge University Press, 2004.